metals

MDPI

Article

Optimizing Rolling Strategies for API 5L X80 Steel Heavy Plates Produced by Thermomechanical Processing in a Reversible Single-Stand Mill

Luiz Gustavo de Oliveira Abreu [1], Geraldo Lúcio de Faria [2], Ricardo José de Faria [3], Daniel Bojikian Matsubara [3] and Rodrigo Rangel Porcaro [2,*]

[1] Gerdau Ouro Branco, Rolling Mill, Ouro Branco 36420-000, Minas Gerais, Brazil
[2] Metallurgical and Materials Engineering Department (DEMET), Escola de Minas, Universidade Federal de Ouro Preto, Ouro Preto 35400-000, Minas Gerais, Brazil; geraldofaria@ufop.edu.br
[3] Gerdau Ouro Branco, Research and Development, Ouro Branco 36420-000, Minas Gerais, Brazil
* Correspondence: rodrigo.porcaro@ufop.edu.br

Abstract: This study focuses on advancing the production of predominantly bainitic heavy plates to meet the API 5L X80 standard. The investigation involves a thorough evaluation of the influence of rolling parameters and austenite conditioning on both microstructural characteristics and mechanical properties. Accurate specifications for chemical composition, processing temperatures, and mean deformations were established using mathematical models and bibliographical references. Four rolling conditions were performed in a reversible single-stand mill, allowing for comprehensive comparison and critical analysis. Microstructural and mechanical characterizations were performed utilizing several techniques, including optical microscopy (OM), scanning electron microscopy (SEM), tensile tests, Charpy impact tests, and hardness tests to ensure adherence to API 5L standards. Additionally, the SEM-EBSD (electron backscattered diffraction) technique was employed for a complementary analysis. The EBSD analysis included crystallographic misorientation maps, mean kernel misorientation parameters (ϑ), low- and high-angle grains boundaries, mean equivalent diameter, and evaluation of the contribution of different strengthening mechanisms to yield strength. Results underscored the significant influence of austenite conditioning on both microstructure and mechanical properties. Considering the specificities of a reversible single-stand mill, it was concluded that, unlike the classic approach for ferritic or ferritic–pearlitic HSLA (high-strength low-alloy steel), when a product with a predominantly bainitic microstructure is required, the accumulated deformation in the austenite during the finishing rolling stage, as well as its temperature, must be meticulously controlled. It was shown that the greater the deformation and the lower the temperature, the more favorable the scenario for the undesired polygonal ferrite formation, which will deteriorate the material's performance. Furthermore, an optimized production route was identified and adapted to the specificities of the employed rolling mill. The presented data have great importance for researchers, manufacturers, and users of API 5L X80 heavy plates.

Keywords: API 5L X80 steel; thermomechanical processing; austenite conditioning; bainitic structure; heavy plate; SEM-EBSD technique

Citation: de Oliveira Abreu, L.G.; de Faria, G.L.; de Faria, R.J.; Matsubara, D.B.; Porcaro, R.R. Optimizing Rolling Strategies for API 5L X80 Steel Heavy Plates Produced by Thermomechanical Processing in a Reversible Single-Stand Mill. *Metals* **2024**, *14*, 746. https://doi.org/10.3390/met14070746

Academic Editor: Frank Czerwinski

Received: 16 April 2024
Revised: 23 May 2024
Accepted: 24 May 2024
Published: 25 June 2024

1. Introduction

The Brazilian demand in the oil and gas sector has witnessed a remarkable growth of approximately 53% in daily oil barrel production over the last decade, especially driven by the pre-salt area [1,2]. Additionally, promising prospects in the natural gas and green hydrogen transportation market, aligned with the European Union's long-term plans for energy transition and climate change mitigation, reinforce the ongoing need for the development of tubes and materials to meet this increasing demand [3–7].

However, the increasingly challenging conditions in the extraction and transportation of hydrocarbons, particularly in adverse environments, with the necessity of transporting larger volumes over extended distances, require tubes with higher mechanical strength and simultaneously elevated toughness. Projects involving larger diameters and increased wall thickness are trends in the pipeline sector [8–11]. Higher wall thickness imposes challenges to meet the demands of tube manufacturers, intensifying the need for significant advancements in material development that comply with stringent standards [8–11].

The continuous research endeavor for steels with high mechanical strength, elevated toughness, and decreasing levels of carbon equivalent has prompted the development of the controlled rolling followed by the accelerated cooling strategy, or TMCP (thermomechanical controlled process). While this approach refines the grain size after controlled rolling, compensating for the alteration in chemical composition, its high implementation cost has limited widespread adoption [12–16]. In Brazil, API 5L X80 steel pipes produced through the TMCP production route exhibit an acicular microstructure predominantly composed of bainite, associated with low carbon content, and microalloying with niobium, vanadium, and titanium [15,17].

The development of X80 (and superior grades) pipeline steels with wall thickness greater than 16 mm is recent [8,15,18,19]. As pointed out by Zhang et al. [8], the increase in thickness of the plate greatly increases the difficulty of controlling the rolling process and the accelerated cooling after rolling. Ensuring the microstructural homogeneity along the heavy wall plates of API pipeline steels is also an engineering challenge for steel manufacturers [15,20,21].

The design of an alloy seeking the manufacturing of API 5L grade X80 heavy plates must meet certain requirements to ensure good weldability and mechanical performance after controlled thermomechanical processing. In this context, many researchers agree that bainitic microstructures obtained from a steel chemical composition that meets $\leq$0.07%C, $\leq$1.85%Mn, $\leq$0.085%Nb, <0.025%Ti, $\leq$0.35%Mo, and $\leq$0.6%Cr (with the possibility of small additions of Ni and V) represent a significant opportunity to achieve the desired product [15,22,23]. According to these authors [15,22,23], for the attainment of X80 grade in low-carbon steels microalloyed with Nb and Ti, as well as containing additions of Mo and Cr, it is crucial to optimize the controlled rolling process: (i) the reheating temperature must be precisely calculated to maximize the effects of Nb and Ti in austenite solid solution during the roughing stages; (ii) the starting and ending temperature of the finishing rolling must be well defined to promote adequate austenite "pancaking", and finally, (iii) the accelerated cooling (cooling rate and final cooling temperature) should be designed to optimize the hardening mechanisms through phase transformation (dislocation and interface density) grain refinement and precipitation.

The proper planning of controlled thermomechanical rolling for the development of API 5L X80 heavy plates becomes even more challenging when a reversible single-stand mill is used. Due to the reversible nature of the equipment, the time between deformation passes is longer than in a multiple-stand sequential system [13,15,24]. This, combined with the application of successive deformations in different directions, alters the kinetics of austenite recrystallization during the roughing stage, as well as modifies the dislocation distribution in austenite after finishing rolling compared to a multi-stand mill. As a result, during accelerated cooling, the kinetics of austenite decomposition will also be affected [13,15,24]. Due to these characteristics, significant process adjustments are necessary, particularly concerning the roughing and finishing pass temperatures, as well as the levels of deformation applied in these stages. For this type of mill, the literature is still very sparse in describing the relationships between process variables, microstructure, and mechanical properties of API 5L X80 heavy plates. The limited available literature, along with industrial reports, indicates the recurrent occurrence of issues related to microstructural heterogeneity in this type of product when manufactured in a mill with reversible characteristics. A major problem is the formation of a significant fraction of polygonal ferrite in a microstructure that should be predominantly bainitic [15].

To better understand this relationship between process variables, microstructure and mechanical properties in thermomechanical controlled processing, in-depth microstructural characterization of rolled products has become essential to accurately describe microstructural features at the phase and constituent classification level, as well as to understand better the contributions of various hardening mechanisms in the material [25–28]. The electron backscattered diffraction (EBSD) technique has consolidated itself as an important tool for characterizing thermomechanically processed products, enabling the quantification of the mean size of crystallographic units, nature of grain boundaries, and low- and high-angle grain boundary discontinuities. This allows the assessment of different hardening mechanisms, such as microstructural refinement, solid solution, precipitation, and increased density of dislocations, to estimate the tensile yield strength, a critical parameter according to API standards [25–28].

In this context, by utilizing an industrial facility and various characterization techniques, including EBSD, this article evaluates and describes the effects of different controlled rolling parameters on the microstructure and mechanical properties of an API 5L grade X80 steel manufactured in a reversible single-stand plate mill. The focus of this study was to evaluate the effect of several austenite conditionings, primarily by altering the finishing rolling conditions, on the steel's microstructure homogeneity. Considering the specificity of the investigated reversible mill, the occurrence of undesired polygonal ferrite in this steel class was first explained as a function of the processing parameters.

2. Materials and Methods

2.1. Materials

For this study, four steel plates were produced from three batches that met the chemical composition ranges presented in Table 1. In addition, the equivalent carbon (*EC*) values—*IIW* and P_{cm}—were also calculated and pointed, according to Equations (1) and (2) [29].

$$EC_{IIW} = \%C + \frac{\%Mn}{6} + \frac{\%Cu + \%Ni}{15} + \frac{\%Cr + \%Mo + \%V}{5} \quad (1)$$

$$EC_{Pcm} = \%C + \frac{\%Si}{30} + \frac{\%Mn + \%Cu + \%Cr}{20} + \frac{\%Ni}{60} + \frac{\%Mo}{15} + \frac{\%V}{10} + 5\%B \quad (2)$$

Table 1. Chemical composition of the plates produced from the three steel batches (wt.%).

Batches	C	Mn	Si	Cr + Mo + Ni	Nb + Ti	Others	EC_{IIW}	EC_{Pcm}
1	0.06	1.81	0.33	0.51	0.049	0.0595	0.46	0.19
2	0.06	1.84	0.25	0.53	0.050	0.0564	0.47	0.19
3	0.05	1.83	0.24	0.60	0.045	0.0632	0.47	0.18

The dimensional target for the manufactured heavy plate was 20.6 mm of final thickness and 1776 mm of final width, starting from a slab 250 mm thick and 1585 mm wide.

2.2. Rolling Parameters and Conditions

Once the chemical composition was defined, the first step considered in planning the controlled rolling process was the determination of plate reheating temperature. This determination was carried out using the decision algorithm proposed by Gorni [30] to choose the most suitable solubilization model based on the approaches established by Irvine et al. [31], Nordberg and Arronson [32], and Hudd et al. [33].

The rolling parameters and conditions (Table 2) were established based on a literature review [8,34] and simulations using the MicroSim-SM® software, as described by Uranga et al. [35]; this software models the microstructural evolution of austenite during

the rolling process. These analyses were crucial for optimizing rolling strategies, aiming for greater refinement and microstructural homogeneity.

Table 2. Target rolling conditions for the manufacture of 20.66 mm heavy plates that comply with API 5L X80 requirements.

Reheating Temperature (°C)	>1100
Sketch Thickness (mm)	70–90
Temperature of the First Finishing Pass (°C)	930–870
Temperature of the Last Finishing Pass (°C)	850–790
Accelerated Cooling Rate (°C/s)	10–20

As illustrated in Figure 1, two distinct rolling strategies, denominated A and B, were implemented using four plates (two for each strategy). Rolling Strategy A involved seven roughing passes and six finishing passes applied to plates 1 and 2, while Strategy B entailed seven roughing passes and eight finishing passes for plates 3 and 4. To achieve approximately equal total deformations of approximately 62% in the roughing stage and 74% in the finishing stage for both strategies, it was necessary to increase the deformation per finishing pass in Strategy A compared to Strategy B. This variation in the rolling scheme constituted a pivotal factor. The target was to maintain a waiting rough thickness (between roughing and finishing) of 80 mm for all four rolling experiments. Depending on the final product thickness, it is customary to apply between 40% and 75% deformation in the roughing and finishing stages, respectively. This approach aims at developing steels with high mechanical strength for applications in the oil and gas industry. Consequently, the total strain values for both stages were defined within the specified range [36].

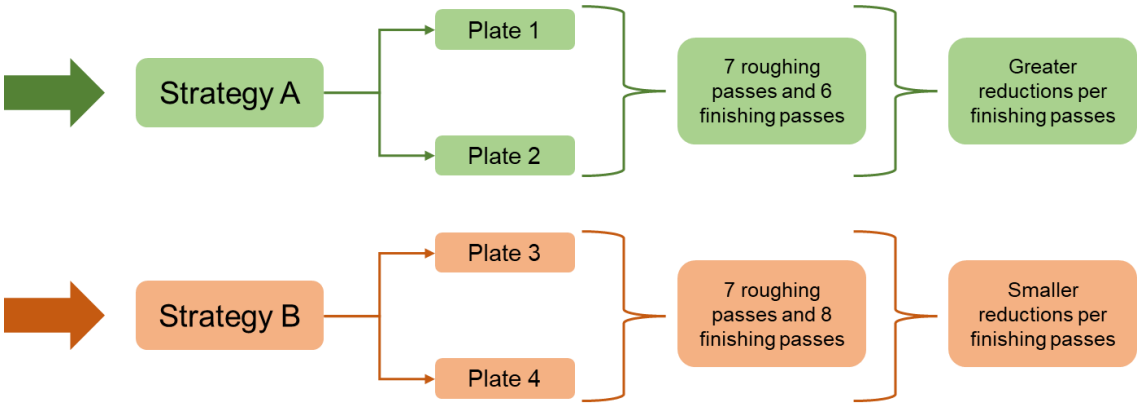

Figure 1. Schematic figure illustrating the two defined rolling strategies.

2.3. Microstructural Characterization—OM and SEM

Two techniques were employed for the microstructural characterization of the manufactured plates: optical microscopy (OM) and scanning electron microscopy (SEM). Microstructural assessments were performed (i) at the center and (ii) at ¼ of the thickness.

Optical microscopy (OM) was employed as a preliminary analysis technique to complement the qualitative characterization of Mn microsegregation, revealing bands of positive segregation of this element. Teepol etchant was utilized, comprising 5 g of picric acid, 0.4 mL of HCl, 30 drops of neutral detergent, and 240 mL of water, with an average etching time of 11 min. Following this, samples underwent a brief etching with Nital 2% to enhance microsegregation contrast and reveal the overall microstructure.

OM was further employed for the characterization of M-A islands (martensite-retained austenite constituent), confirming their existence and evaluating their fraction and mean size. Metallographic sample preparation followed ASTM E3 standard recommenda-

tions [37], and Klemm etchant was used for etching. This etchant's stock solution consisted of 30 g of saturated sodium thiosulfate diluted in 60 mL of water. This dilution was performed hot, between 30 °C and 40 °C, and then the solution was stored at room temperature for 3 h.

A working solution, comprising 2 g of potassium metabisulfite in 40 mL of water, was mixed with the stock solution. The samples were then etched by immersion for 2 min. Subsequently, an optical microscope (LEICA DM2700M, Leica Microsystems GmbH, Wetzlar, Germany) was utilized for imaging at 500× and 1000× magnifications. ImageJ software–version 1.53–was applied for image processing, and the volumetric fraction of M-A islands was measured.

SEM was employed on plates 4 and 1 from the same batch and rolling conditions to verify constituents and characterize M-A islands at 5000× magnification, using a TESCAN VEGA 3 SEM (TESCAN, Brno, Czech Republic). Nital 2% etchant was applied to reveal constituents and assess M-A islands.

Three scenarios were considered for measuring M-A island fractions and average size: (a) quantification using OM at 500× magnification (Klemm etchant); (b) OM with 1000× (Klemm etchant); (c) SEM with 5000× (Nital 2% etchant). Image processing in ImageJ and quantitative metallography procedures recommended by ASTM E112 [38], ASTM E1245 [39], and ASTM E562 [40] standards were applied in all scenarios, to ensure the representativeness of the obtained data; the numbers of sampled fields must ensure a relative precision of less than 10%, as per Equation (3), and the 95% confidence interval (95% CI), given by Equation (4).

$$\%RA = \frac{95\%\cdot CI}{\overline{x}} \cdot 100 \tag{3}$$

$$95\%\cdot CI = \frac{t\cdot s}{\sqrt{n}} \tag{4}$$

In these equations, n represents the number of evaluated fields; t is the t-Student statistical parameter obtained from the tables of ASTM E112 [38], ASTM E1245 [39], and ASTM E562 [40] standards as a function of the number of fields n. Finally, s is the standard deviation related to the measured values, and $\overline{x}$ is the average fraction of the M-A constituent.

It is worth noting that two different methodologies for quantifying phase fractions through image analysis were employed. One involves estimating the volumetric fraction (%) of the M-A constituent using the area method. In this method, for each of the evaluated images (for the three scenarios (a), (b), and (c)), the area of the micrograph corresponding to the M-A islands was determined, and its fraction (%) relative to the total area of the micrograph (parameter A_A) was calculated. According to ASTM E112 [38], ASTM E1245 [39], and ASTM E562 [40], if the A_A parameter (Equation (5)) is determined such that $\%RA < 10\%$ (relative accuracy), it is a good indicator of the volumetric fraction (%) of the M-A constituent.

$$A_A = \frac{Areas\ of\ the\ M-A\ islands}{Total\ Area\ of\ the\ Micrograph} \tag{5}$$

For the same images used in the calculation of parameter A_A, parameter P_A (Equation (6)) was also calculated. This parameter calculates the density of *M-A* islands per unit area, i.e., for each of the micrographs that were analyzed, it counts how many *M-A* islands are present and divides the number of islands by the total area of the micrograph. When considering two or more magnifications such that the resolution power of the technique used allows *M-A* islands with the same size range to be observed and counted, this method, considering random and nonrepetitive sampling, should be less sensitive, or even not significantly affected by the magnification used.

$$P_A = \frac{Number\ of\ M-A\ Islands}{Total\ Area\ of\ the\ Micrograph} \tag{6}$$

Seeking to better characterize the *M-A* constituent islands present in the samples, the same images used in the volumetric fraction and island density quantification step were used to determine the size distribution of the islands, as well as to determine the average size. For this purpose, the method of the equivalent diameter standardized by ASTM E112 [38] and ASTM E1382 [41] standards was used. This method was applied automatically with the aid of the ImageJ software. It involved measuring the area of each *M-A* island identified per field. Then, for each of them, it was determined what the circumference with diameter d would be, which would have an area equivalent to the analyzed island. The diameter d of this circumference is then called the average equivalent diameter of the island. This method was applied to each of the identified islands in all fields analyzed from different regions of the samples.

2.4. Microstructural Characterization—SEM-EBSD

Analysis and characterization using the scanning electron microscopy–electron backscatter diffraction (SEM-EBSD) technique was performed on plate 2 (Strategy A) and plate 4 (Strategy B), at ¼ of the thickness. The tests were carried out using a e Philips XL 30CP SEM with a W-filament, using TSL (TexSEM Laboratories, Salt Lake City, UT, USA) equipped with an EBSD module and a PEGASUS 4000 system (TSLEDAX, Warrendale, PA, USA).

Several imaging techniques were employed, including the inverse pole figure, crystallographic misorientation maps, and kernel average misorientation (KAM) maps ($\vartheta < 2^\circ$), alongside their respective mean kernel misorientation parameters (ϑ). Grain boundary maps were generated to highlight the fractions and sizes of grains with low-angle boundaries ($4^\circ < \vartheta < 15^\circ$) and high-angle boundaries ($\vartheta > 15^\circ$), aimed at assessing the contributions of various strengthening mechanisms to yield strength. Additionally, mean grain sizes were estimated using 4° and 15° angles as threshold criteria.

Based on the information obtained from the EBSD characterization, contributions from different strengthening mechanisms were estimated for the yield strength of both plates, following Equation (7).

$$\sigma_y = f\left(\sigma_{ss}, \sigma_{gs}, \sigma_\rho, \sigma_{ppt}\right) \tag{7}$$

Thus, according to Isasti et al. [25], the yield strength (σ_y) of low-carbon microalloyed steels can be expressed as a combination of different strengthening mechanisms, such as solid solution strengthening (σ_{ss}), grain size strengthening (σ_{gs}), dislocation density strengthening (σ_ρ), and fine precipitation strengthening (σ_{ppt}).

Pickering and Gladman [42] proposed Equation (8) to assess the contribution of solid solution strengthening; the commonly adopted value for σ_o is 53.9 MPa, and the concentrations of the elements should be entered as weight percentages.

$$\sigma_{ss} = \sigma_o + 32.3Mn + 83.2Si + 11Mo + 354(N_{free})^{0.5} \tag{8}$$

Several equations have been proposed to calculate the contribution related to grain size. The most suitable one for bainitic products microalloyed with Nb and Mo addition, such as the alloy in this article, would be Equation (9) proposed by Iza Mendia and Guitiérrez [43]. This equation is considered more appropriate because it considers that the contribution of each grain boundary, or sub-boundary, depends on its crystallographic misorientation angle.

$$\sigma_{gs} = 1.05\alpha M\mu\sqrt{b}\left[\sum_{2^\circ \le \theta_i \le 15^\circ}\left(f_i\sqrt{\theta_i}\right) + \sqrt{\frac{\pi}{10}}\sum_{\theta_i \ge 15^\circ}(f_i)\right].\, d_{2^\circ}^{-0.5} \tag{9}$$

The first term of Equation (7) corresponds to the contribution of low-angle boundaries, and the second term corresponds to the contribution of high-angle boundaries. The parameters θ_i and f_i represent the mean misorientation angle, in radians, in the "i" interval, and the relative frequency, respectively. The parameter d_{2° is the mean equivalent diameter (MED) considering the threshold angle criterion of 2°. For Equations (9) and (10), α is a constant (0.3), M is the mean Taylor factor (3), μ is the shear modulus (8×10^4 MPa), and b

is the magnitude of the Burgers vector ($b = 2.5 \times 10^{-7}$ mm). The contribution related to the dislocation density strengthening can be expressed through Equation (10).

$$\sigma_\rho = \alpha M \mu b \sqrt{\rho} \tag{10}$$

Finally, ρ is the dislocation density, and according to Kubin and Mortensen [44], they proposed a model to calculate the dislocation density (ρ) from KAM maps data obtained by EBSD (Equation (11)), where μ is the length unit (1.86 times the step size used in the EBSD analysis), and b is the Burgers vector. The parameter ϑ is the mean kernel misorientation value. For the determination of ϑ and, consequently, the contribution relative to the dislocation density, as mentioned, values of $\vartheta < 2^\circ$ should be considered.

$$\rho = \frac{2\vartheta}{ub} \tag{11}$$

Considering the actual yield strength (σ_y) can be readily measured through tensile testing, some authors, such as Zurutuza et al. [45], use Equation (7) to determine the contributions of each strengthening mechanism to the yield strength. However, they did not calculate the precipitation contribution due to challenges in quantifying the fraction and size of precipitates. In this context, they introduced a parameter, σ_{us} (unaccounted strength), representing the difference between the experimentally measured yield strength and the contributions from dislocation density, grain size, and solid solution. According to the authors, this difference (σ_{us}) would be associated with (1) a specific effect of carbon in solid solution in only quenched samples and (2) the strengthening effect of carbide precipitation of Nb and Mo in quenched and tempered samples.

Therefore, in this study, owing to the complexity of quantifying the volume fraction of precipitates, the precipitation contribution was estimated by calculating the difference between the experimental yield strength and the remaining contributions: solid solution (Equation (8)), grain refinement (Equation (9)), and dislocation density (Equations (10) and (11)), as carried out by Zurutuza et al. [45], respectively, for plates 2 and 3. It is noteworthy that the effect of the M-A constituent fraction, expected to be negligible and similar in both plates, was disregarded in the contribution calculation [25–28].

2.5. Mechanical Tests

To determine the yield strength (YS), tensile strength (TS), total elongation, impact toughness, and material hardness values, we carried out tensile tests, Charpy impact tests, and hardness tests following the ASTM A370 [46] and ASTM E92 [47] standards (Figure 2).

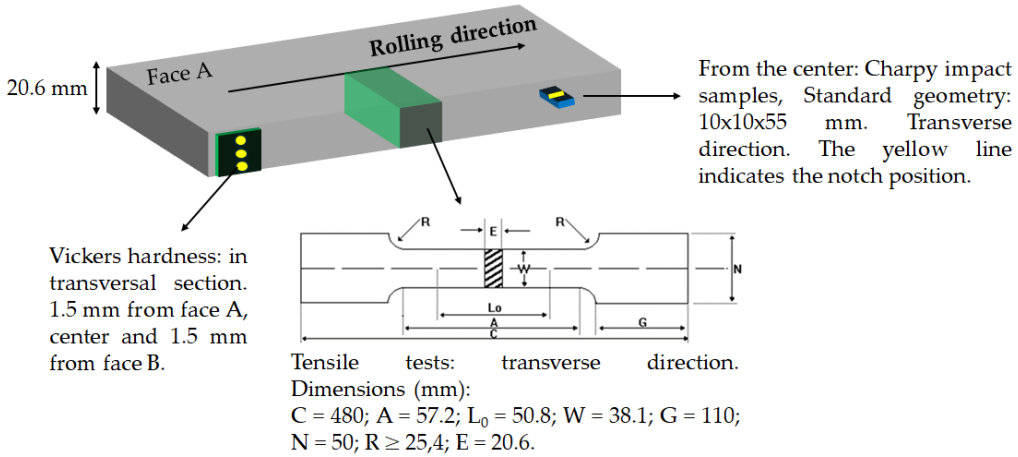

Figure 2. Schematic figure illustrating the mechanical tests performed on samples from heavy plates obtained according to different rolling strategies.

Tensile tests were performed at room temperature using an MTS model machine with 2000 kN capacity. Charpy impact tests were carried out on a ZwickRoell PSW 750 machine (ZwickRoell GmbH & Co., Ulm, Germany) at −20 °C to quantify toughness at temperatures below those defined by the API 5L standard [48]. Finally, hardness tests were conducted at three positions along the thickness (1.5 mm from face A, center, and 1.5 mm from face B) using a Vickers hardness tester with a 1 kgf load. The hardness measurements were performed with a Wilson–Wolpert Durometer, model S8–300, with a maximum capacity of 50 kgf. All tests were carried out at the Gerdau Ouro Branco Test Center, serving as a reference for the API 5L X80 standard, with a focus on PSL 2 specification pipes [48]. All mechanical tests were performed in triplicates.

3. Results and Discussion

3.1. Rolling Results

The results indicated in Table 3 reveal that all four rolling strategies met the solubilization temperature requirement for Nb, around 1150 °C. For this steel chemical composition, this temperature is in accordance with the literature [15,22,23,30,31]. Cumulative deformation in the roughing and finishing stages was approximately 62% and 74%, respectively, for plates 1 and 2 (Strategy A) and 4 (Strategy B). However, a deviation occurred in plate 3 (Strategy B), in which less deformation in the roughing stage resulted in increased cumulative deformation in the finishing stage to achieve the final thickness of 20.66 mm.

Table 3. Comparison of the main rolling parameters applied to the four 20.66 mm thick heavy plates to comply with API 5L X80 requirements.

Parameters	Strategy A		Strategy B	
	Plate 1	**Plate 2**	**Plate 3**	**Plate 4**
Reheating Temperature (°C)	Ts + 43	Ts + 40	Ts + 47	Ts + 46
Roughing Passes	7	7	7	7
Finishing Passes	6	6	8	8
Accumulated Deformation in Roughing (%)	62.2	62.1	**57.6**	62.2
Accumulated Deformation in Finishing (%)	74.2	74.2	**77**	74.2
Temperature of the First Finishing Pass (°C)	T_{nr} − 80	T_{nr} − 80	T_{nr} − 78	T_{nr} − 81
Temperature of the Last Finishing Pass (°C)	A_{r3} + 99	A_{r3} + 96	A_{r3} + 68	A_{r3} + 65
Accelerated Cooling Rate (°C/s)	13	13	15	13

In terms of the temperatures for each stage of the process, it can be affirmed that the target values, as per Table 2, were attained, except for the mean rate of accelerated cooling. However, due to the eight finishing passes with less deformation applied per pass in rolling Strategy B, there were smaller reductions in thickness per finishing pass. Consequently, it was necessary to apply finishing passes at lower temperatures, close to the lower limits allowed, toward the end of this stage. When comparing the final finishing temperatures of the plates subjected to Strategy A with those of Strategy B, a difference of approximately 15 °C is evident. This is particularly emphasized in plate 3, which underwent the highest accumulated deformation in the austenite and obtained the lowest temperature during the last finishing passes. Despite the limited amount of industrial processing data available in the literature, comparing these parameters with the literature, it is possible to observe that considering the classical use of multiple-stand sequential mills for API 5L X80 manufacturing, the accumulated deformation in roughing and finishing stages are, in general, lower than those herein employed, mainly in finishing rolling [15,23,34]. The reversible mill, based on Microsim software simulations [35], employed 7 roughing passes and 6–8 finishing passes. Studies on a sequential rolling system indicate the use of 4 to 5 passes each for roughing and finishing, resulting in a smaller total thickness reduction

relative to the initial slab dimensions [18]. In this context, it is possible to affirm that there is significant process difference between reversible single-stand and multi-stand mills aiming to manufacture X80 heavy plates.

Concerning the cooling rate, despite the target value being 16 °C/s, it is observed that the rate achieved in Strategy A was 13 °C/s. In Strategy B, where finishing passes were applied at lower temperatures, the achieved rates were 15 °C/s and 13 °C/s for plates 3 and 4, respectively, given that the results correspond to experiments conducted on an industrial scale, the deviation in the cooling rate values for the experiment falls within the process variation range.

With cooling rates between 13 °C/s and 15 °C/s, significant granular bainite formation may occur under all conditions [8,15,18]. However, considering the effect of accumulated strain in austenite and dislocation density on austenite decomposition kinetics, the formation of polygonal and quasi-polygonal ferrite becomes possible [15,49]. Additionally, there is a tendency for a greater fraction of M-A islands to occur in the plates of Strategy B, especially in plate 3 [34].

3.2. Microstructural Characterization Results—OM and SEM

Figures 3 and 4 depict the microstructure evaluation results obtained through optical microscopy (OM) at the ¼ thickness and central thickness positions. The images are presented at original magnifications of 500× and 1000×, illustrating the microstructural characteristics of the four rolled plates.

Observing the micrographs presented in Figures 3 and 4, it was possible to discern some relevant aspects. Plates 1 and 2 (Strategy A) predominantly exhibited bainitic microstructures with a granular appearance. Regarding the central position of plates 3 and 4 (Strategy B), as depicted in Figure 4, it was observed that in plate 3, the microstructure predominantly transformed into bainite, with no observable polygonal ferrite through optical microscopy. As for plate 4, bands consisting of polygonal ferrite were still evident, although in a smaller fraction compared to that observed at ¼ of the thickness. The central region of rolled plates with relatively high manganese content typically exhibits a broader zone of positive manganese segregation. Consequently, the retarding effect of manganese on austenite decomposition would make the formation of polygonal ferrite difficult in these regions [15,18,50].

Figure 5 shows the SEM micrographs of plates 4 and 1 at the central and ¼ thickness positions, respectively. The microstructures observed in both plates, consistent with OM characterization, are predominantly bainitic. Notably, in both cases, the microstructures exhibit a slightly finer refinement at the ¼ thickness position compared to the central region. This phenomenon is attributed to the central region of rolled plates having a temperature above the nonrecrystallization temperature (T_{nr}) in contrast to the surface-proximate region, indicating a static recrystallization regime [24].

In Figure 5, a comparison reveals that the granular bainite blocks in plate 1 are slightly smaller than those observed in plate 4. This difference can be attributed to both the deformation accumulated at low temperatures in plate 4 and the smaller austenitic grain size in plate 1, leading to an increased number of sites available for bainite nucleation. With a higher nucleation rate and lower transformation temperature, the bainite microstructure tends to be more refined. However, plate 4 exhibits a significantly higher fraction of polygonal ferrite than plate 1. This suggests a leftward shift in the continuous cooling transformation (CCT) diagrams for plate 4 compared to those of plate 1 [49]. Considering that plate 4 was cooled at a mean rate of 13 °C/s, favorable thermodynamic and kinetic conditions were present for the formation of polygonal ferrite, which experiences the lowest cooling rate [8,15]. Additionally, this outcome may imply that the deformation accumulated at low temperatures in plate 4 contributed to the bainite transformation occurring at higher temperatures. Despite the availability of nucleation sites, this led to a structure with granular bainite blocks slightly coarser than those observed in plate 1 [51]. Figure 6 provides a detailed view of the microconstituents identified in plates 4 and 1.

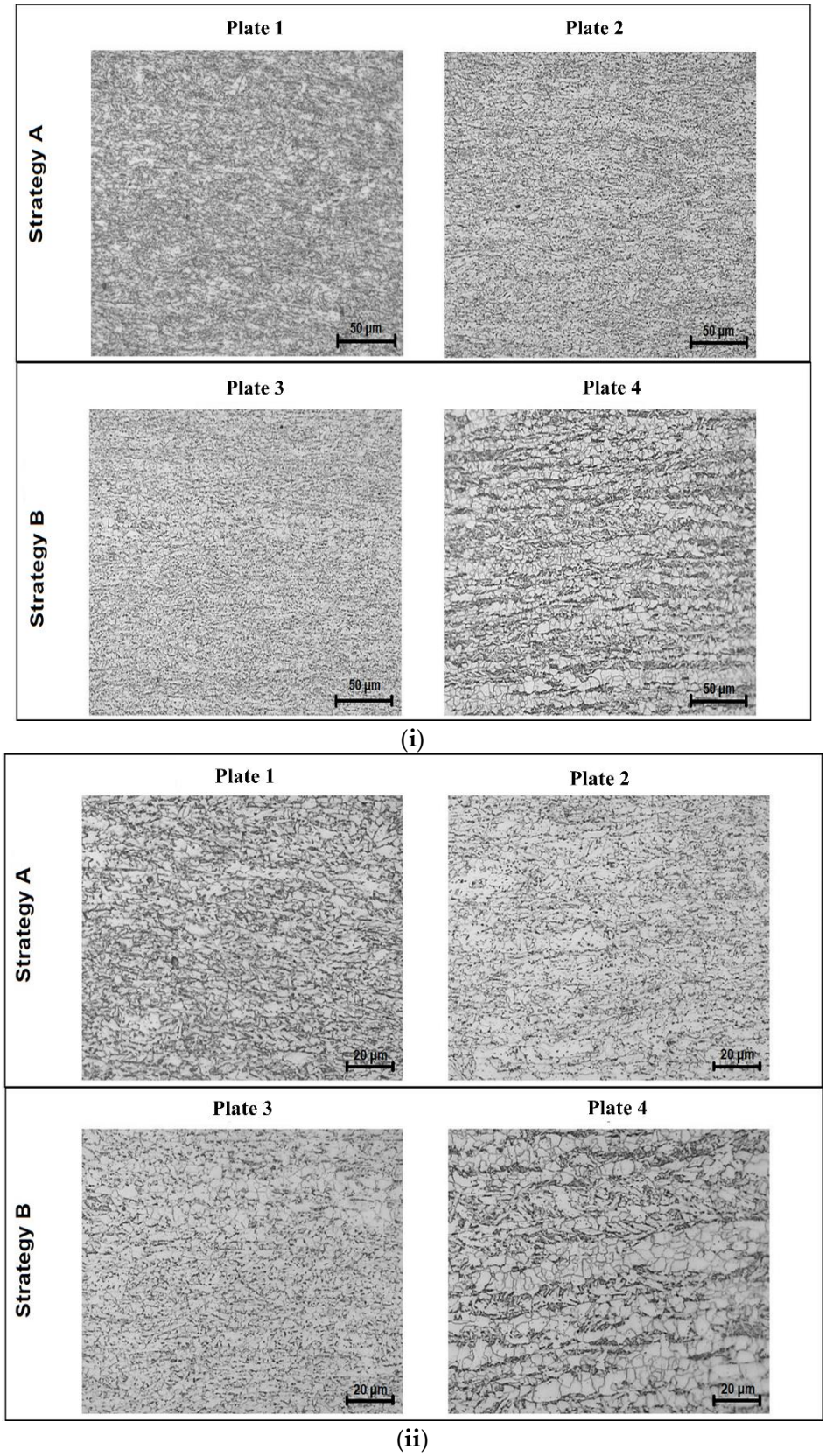

Figure 3. Comparison of microstructures obtained by OM at ¼ thickness position (**i**) 500× and (**ii**) 1000×. Nital 2% etchant.

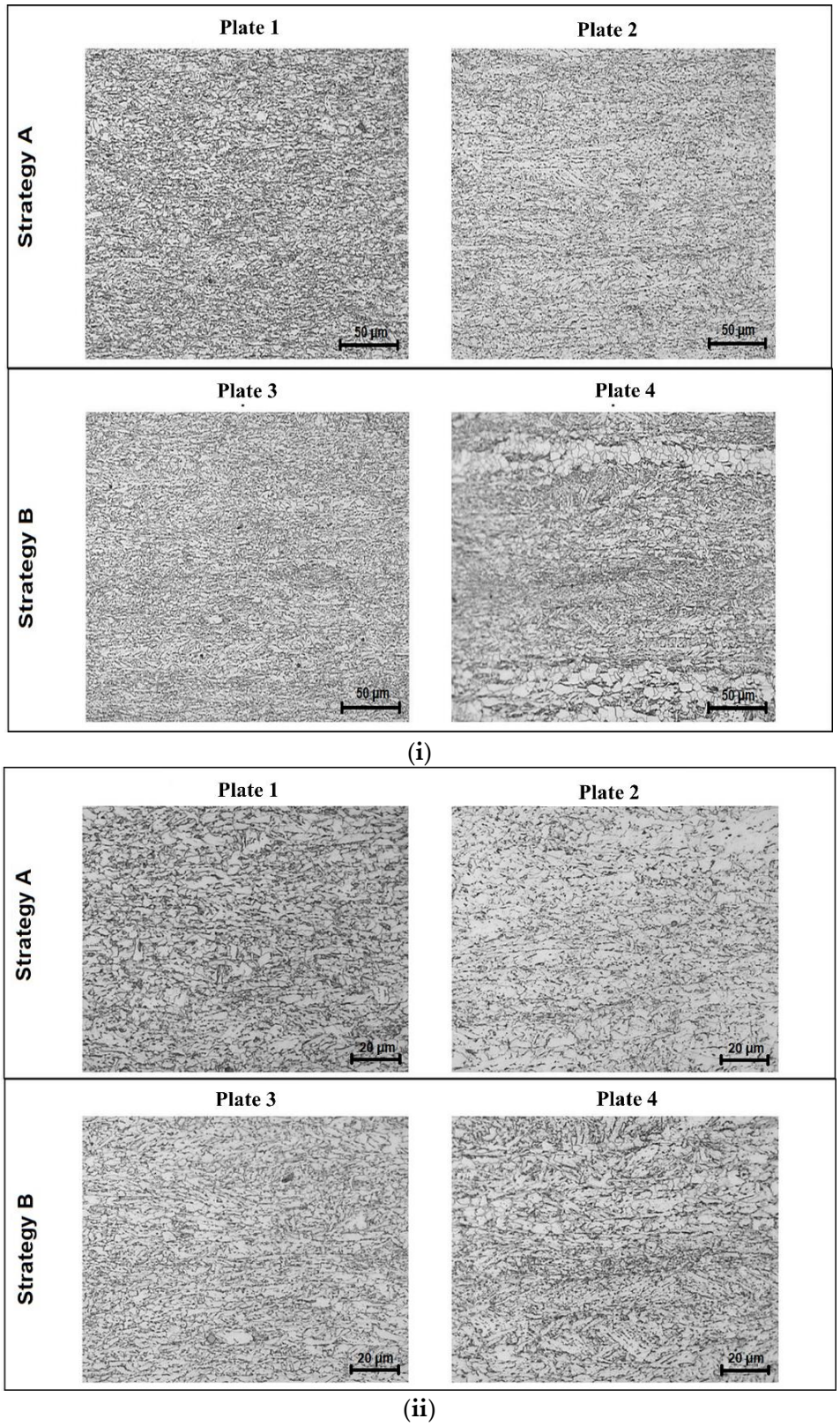

Figure 4. Comparison of microstructures obtained by OM in the central position (**i**) 500× and (**ii**) 1000×. Nital 2% etchant.

Comparing the micrographs depicted in Figure 6, it is evident that the granular bainite blocks are slightly smaller in plate 1. Furthermore, it was observed that there was no formation of degenerate pearlite or superior bainite, which is highly advantageous in terms

of toughness [8]. However, the presence of polygonal ferrite was confirmed, and it is more predominant in plate 4.

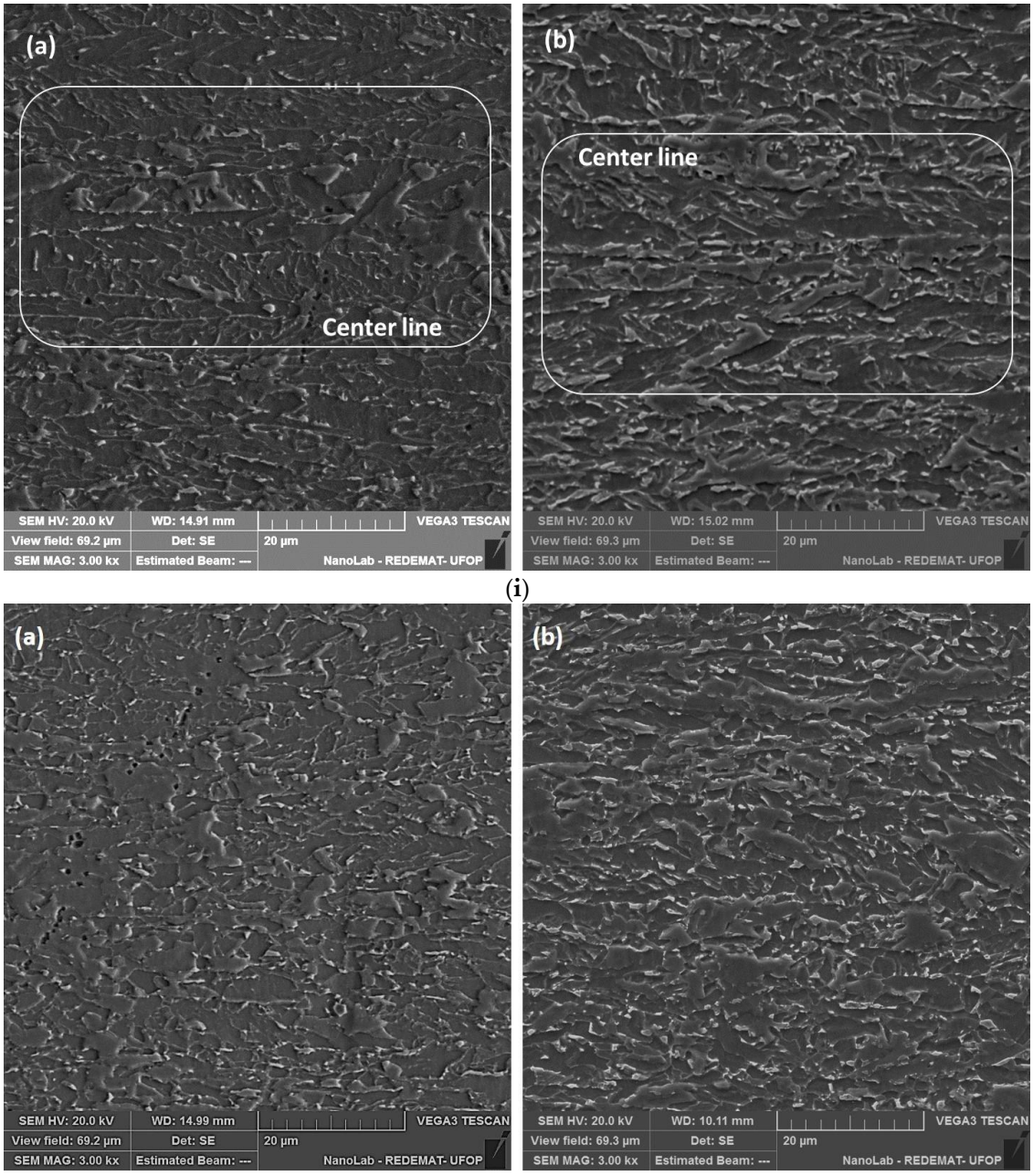

Figure 5. Micrographs obtained by SEM-SE (**i**) of plates (**a**) 4 and (**b**) 1 in the central position (3000×) and (**ii**) of plates (**a**) 4 and (**b**) 1 in the ¼ thickness position (3000×). Nital 2% etchant.

Despite the differences between the process studied here and those described in the literature for multi-stand mills, the microstructures obtained are very similar to those reported by various authors who produced API 5L X80 steel through thermomechanical processing [8,15,18,23,25,34]. Predominantly bainitic microstructures with the occurrence of M-A constituents in blocky or film morphology are described by several authors as satisfactory for this type of product [8,15,18,23,25,34]. However, they highlight that the presence of a significant fraction of polygonal ferrite can act as an undesirable microstructural heterogeneity.

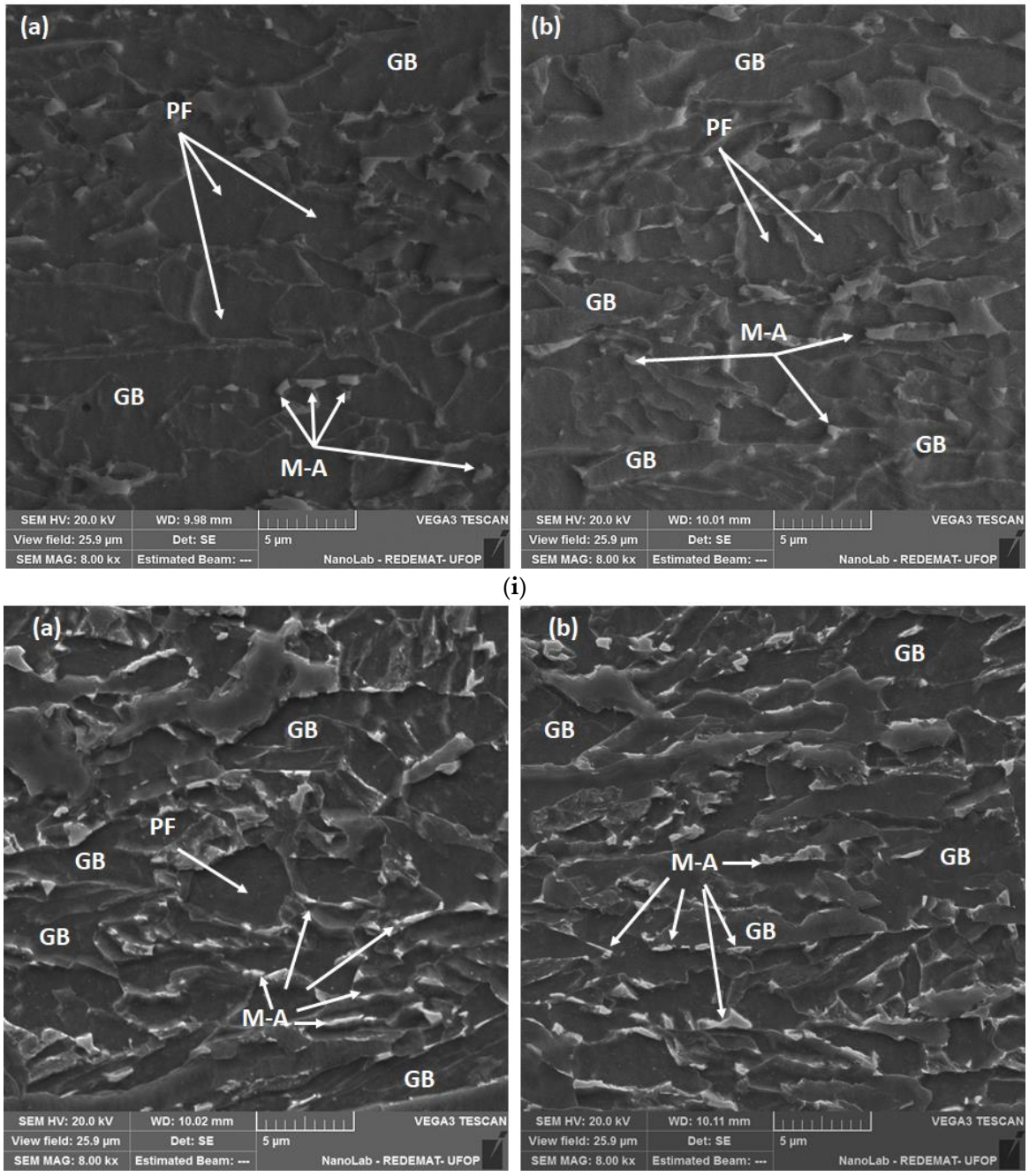

Figure 6. Micrographs obtained by SEM-SE that illustrate details of the microconstituents in plates (**i**) 4 and (**ii**) 1 (**a**) in the center; (**b**) in the ¼ thickness position (8000×)—(polygonal ferrite (PF), granular bainite (GB), M-A islands (M-A). Nital 2% etchant.

3.3. Mn Segregation Results

The micrographs in Figure 7 show the qualitative Mn segregation results obtained for plate 4: (i) at the central region and (ii) at the ¼ of the thickness. There is Mn microsegregation in both the central region and at ¼ of the thickness, but with different characteristics. In the central region, wider bands are observed, but more spaced from each other. At ¼ of the thickness, thinner bands are observed, but closer to each other. Figure 8 presents the results obtained for plate 1: (i) at the central region and (ii) at the ¼ of the thickness.

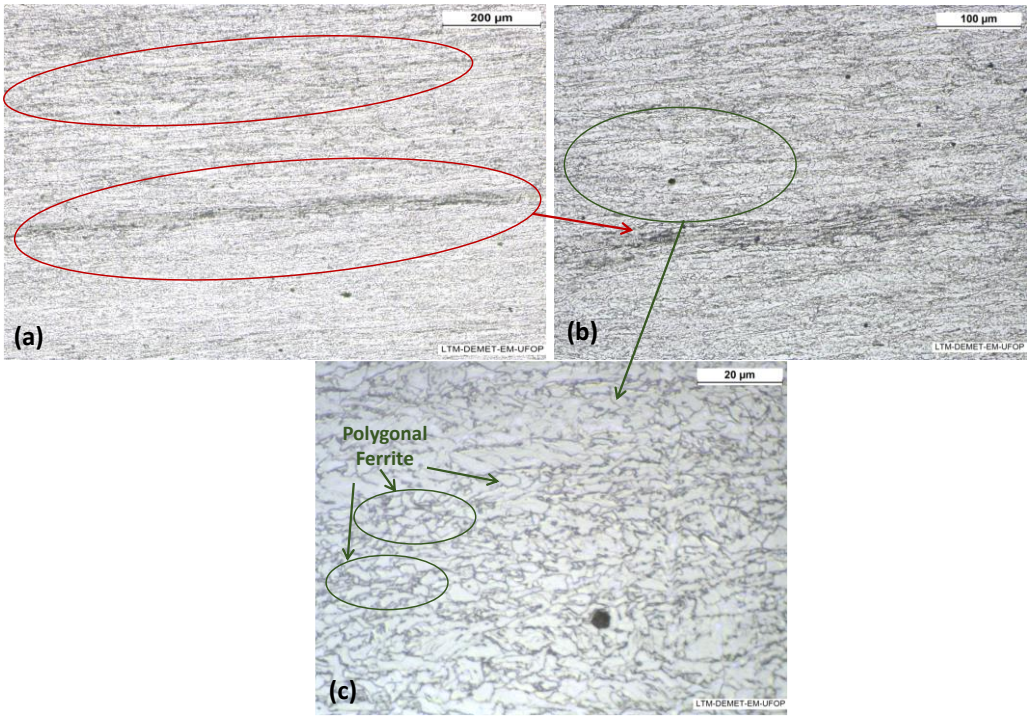

(**i**)

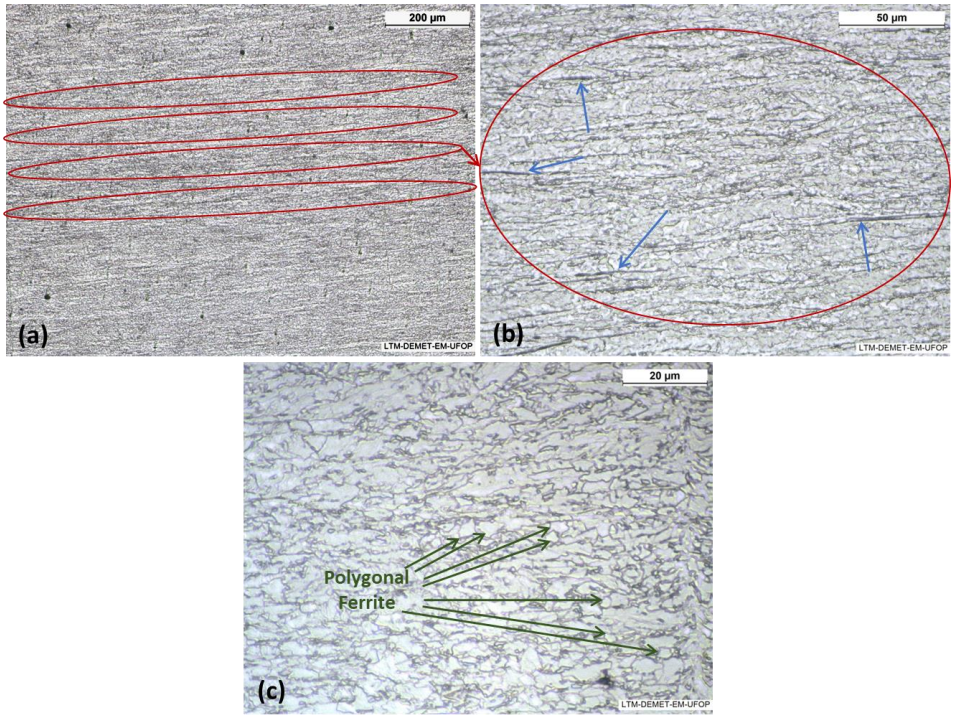

(**ii**)

Figure 7. Micrographs indicating Mn microsegregation (**i**) in the central region and (**ii**) at the ¼ thickness position of plate 4: (**a**) OM—100×; (**b**) OM—500×; (**c**) OM—1000×. Teepol and Nital 2%.

Similarly to plate 4, Mn microsegregation is also present in both the central region and at ¼ of the thickness in plate 1. This is expected since the two plates come from the same batch and casting conditions. In both plates, wider and more widely spaced bands are observed in the central region, while at ¼ of the thickness, thinner bands closer to each other are observed. As anticipated, polygonal ferrite grains are found in regions of negative segregation, with a seemingly smaller grain size in plate 4. It is worth noting that

in Figures 7(ii-b) and 8(ii-b), when examining the microsegregation regions with greater magnification, islands with very dark contrast aligned in the direction of rolling can be observed. These regions are likely to be particularly enriched in manganese, making them more prone to the formation of refined structures or M-A islands, considering the same cooling rate [15,52].

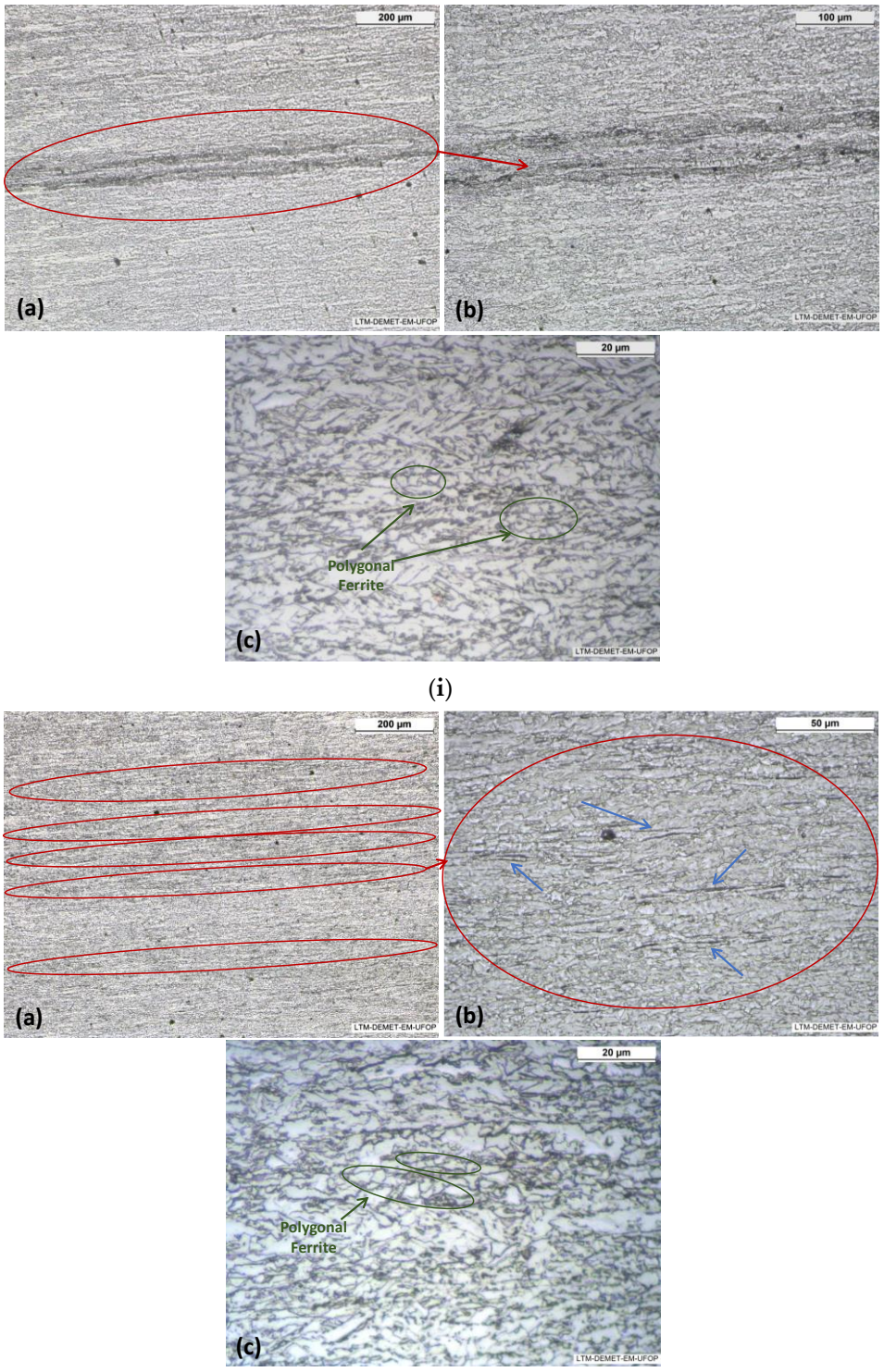

Figure 8. Micrographs indicating Mn microsegregation (**i**) in the central region and (**ii**) in the ¼ thickness position of plate 1: (**a**) OM—100×; (**b**) OM—200×; (**c**) OM—1000×. Teepol and Nital 2%.

In bainitic steels, if there is Mn segregation, the austenite–bainite transformation will occur at lower temperatures than those observed in regions depleted in the element. This could lead to a refinement of the bainitic microstructure in the manganese-enriched regions. Additionally, there is the possibility of an increased occurrence of M-A islands in these regions [15,52].

3.4. M-A Island Characterization Results

Figures 9 and 10 present optical micrographs, respectively, of the central regions and ¼ of the thickness of plates 4 and 1, with magnifications of 500× and 1000×, subjected to Klemm etching. The M-A islands can be observed in the images with a magnification of 500×; the observation of very small M-A islands is challenging. Only the coarser islands can be visualized in both regions, in both plates.

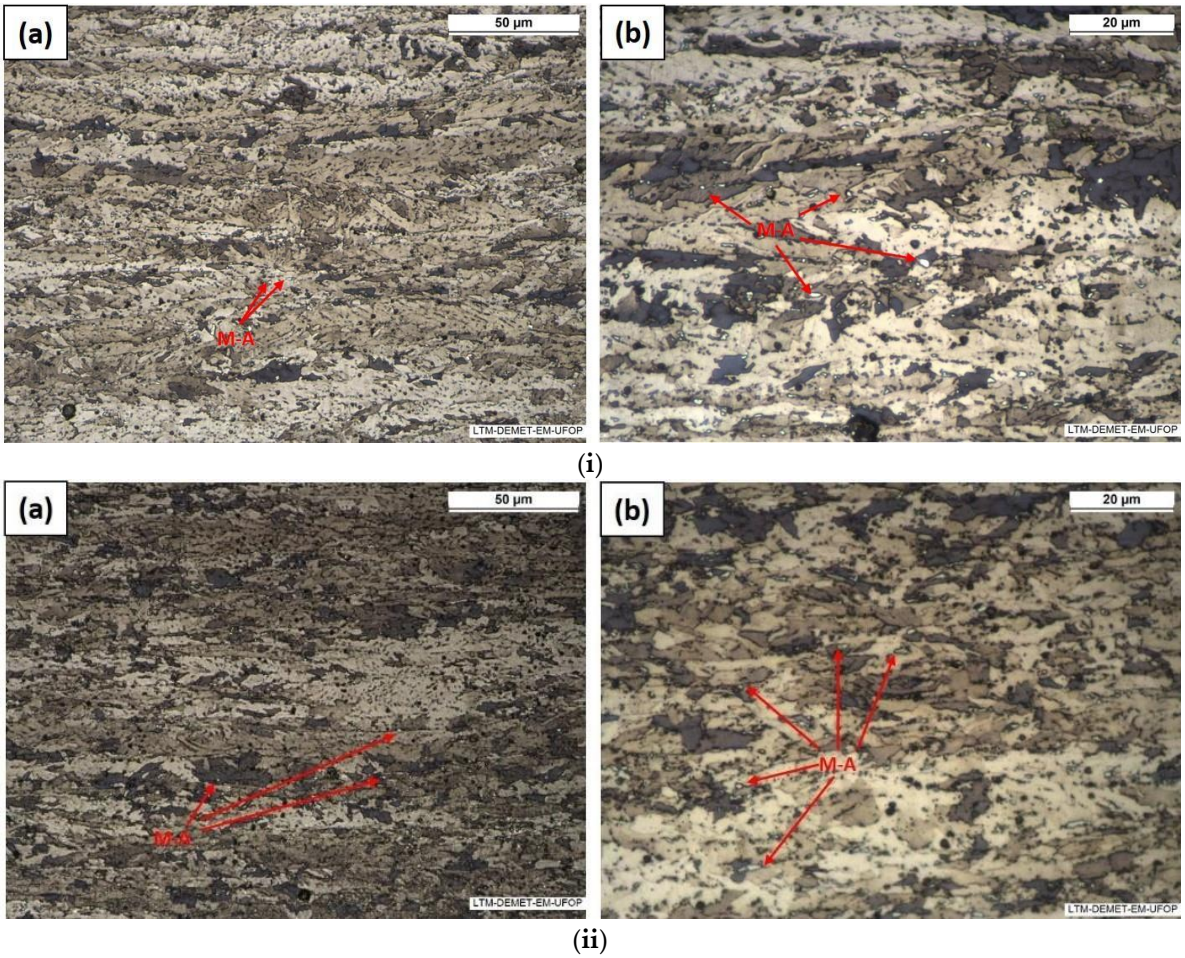

Figure 9. Micrographs obtained by optical microscopy (**i**) in the central region and (**ii**) in the ¼ thickness position of plate 4 illustrating the distribution of M-A islands with magnifications of (**a**) 500× and (**b**) 1000×. Klemm etching.

The SEM characterization of M-A islands in plates 4 and 1 was performed at 5000× magnification. Figure 11 presents examples from the central positions and at ¼ of the thickness for plates 4 and 1, respectively.

Figure 11 shows the M-A islands present in both plates, revealing a significant fraction of M-A islands smaller than 0.6 µm, which was not observable with 500× magnification in OM. Notably, the M-A islands tend to be situated predominantly at the boundaries of granular bainite blocks, exhibiting both blocky and elongated appearances in different regions.

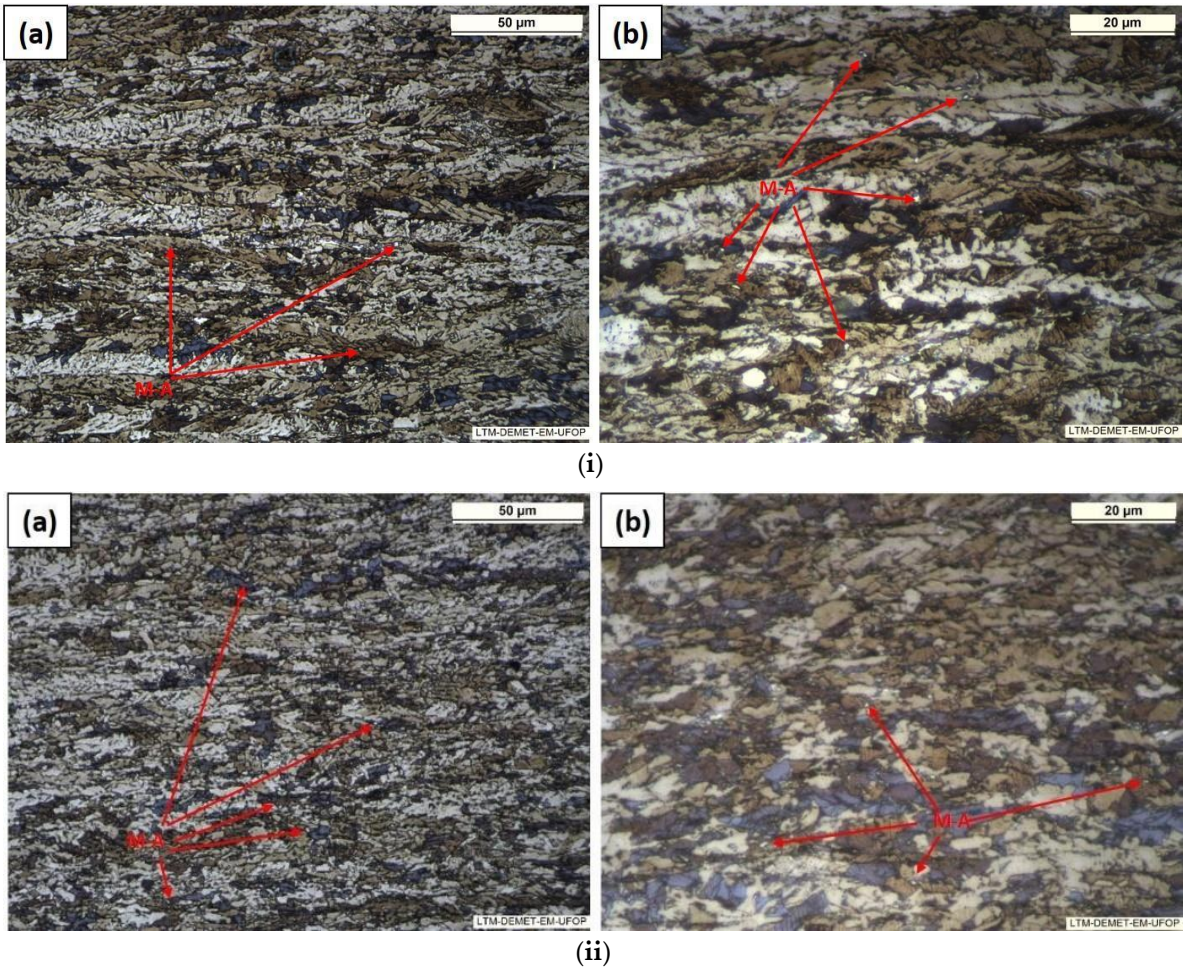

Figure 10. Micrographs obtained by optical microscopy (**i**) in the central region and (**ii**) in the ¼ thickness position of plate 1 illustrating the distribution of M-A islands with magnifications of (**a**) 500× and (**b**) 1000×. Klemm etching.

Figure 12 provides a comparative analysis of the densities (P_A) and volumetric fractions (%) (A_A) of M-A islands in the central regions and at ¼ of the thickness for plates 4 and 1. Generally, the M-A island fractions in both plates across the investigated regions are relatively low. SEM images show the largest fractions, reaching a maximum volumetric fraction of around 2.6%. It is important to highlight that quantifications from optical micrographs appear to underestimate both the volumetric fraction (%) and the density (μm^2) of M-A islands. Takekazu et al. [53] reported volumetric fractions of approximately 5% for M-A islands in heavy plates used for API 5L X80 pipe production. However, given that M-A islands are characterized by regions of high hardness, they may contribute to both ductile and brittle fracture mechanisms [15,23,53–55].

M-A islands function as significant stress concentrators, potentially aiding in crack propagation through cleavage. There is substantial evidence indicating that this type of crack tends to propagate preferentially along the M-A/matrix interface. In this context, smaller M-A islands will exhibit fewer stress fields in their vicinity when the material is subjected to mechanical stress, thereby reducing the likelihood of serving as preferred sites for crack nucleation [54–56]. If these more refined M-A islands are not closely positioned or aligned with each other in the previous austenitic grain boundaries, they can act as beneficial elements by retarding crack propagation. This occurs by increasing tortuosity in the propagation path. In a related study [55], the authors noted that massive M-A islands delayed cleavage-induced crack propagation by creating barriers to growth or deviating the crack from its original direction.

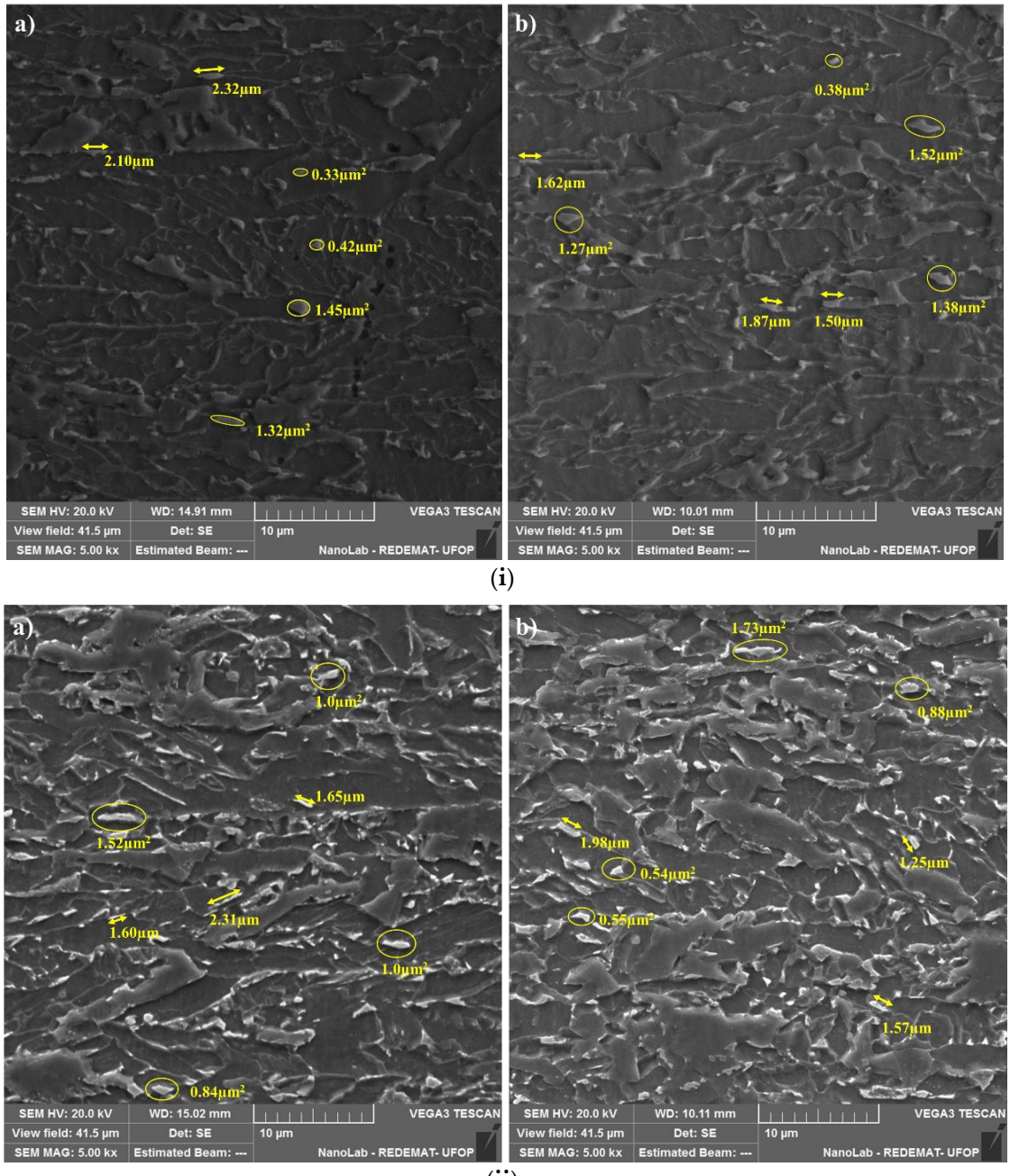

Figure 11. SEM micrographs depicting the distribution of M-A islands at (**a**) the center of the thickness and (**b**) ¼ of the thickness for plates (**i**) 4 and (**ii**) 1, captured at a magnification of 5000×. Nital 2% etchant.

Figure 13 presents a comparison between the average equivalent diameters of M-A islands measured through the application of three evaluated methodologies. Both in the center and at the ¼ thickness position, for the two plates evaluated, it is observed that the OM technique overestimates the sizes of M-A islands, especially at a magnification of 500×, making it unreliable for this type of assessment. When considering measurements made using SEM, it is observed that, for plate 4, the average equivalent diameter at the central and ¼ thickness positions is 0.35 µm and 0.36 µm, respectively. For plate 1, in the same positions, they are identical and equal to 0.29 µm.

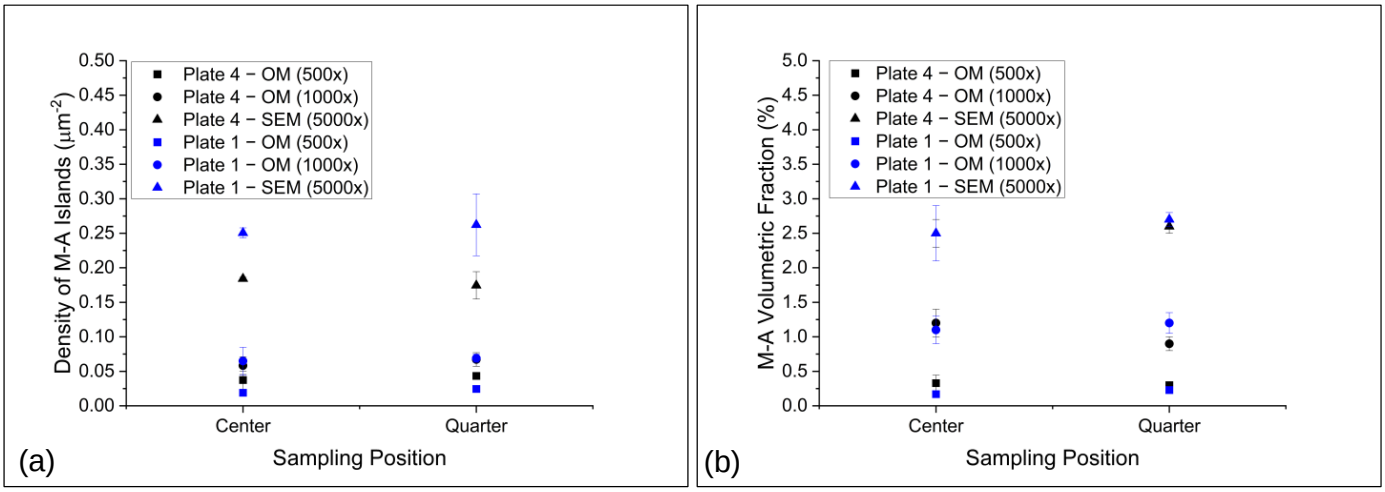

Figure 12. Comparison between the fractions of M-A islands quantified in the central positions and at ¼ of the thickness of the 4 and 1 plates using OM with magnifications of 500× and 1000×, and using SEM with magnification of 5000×: (**a**) density of islands (P_A), (**b**) volume fraction of islands (%) (A_A).

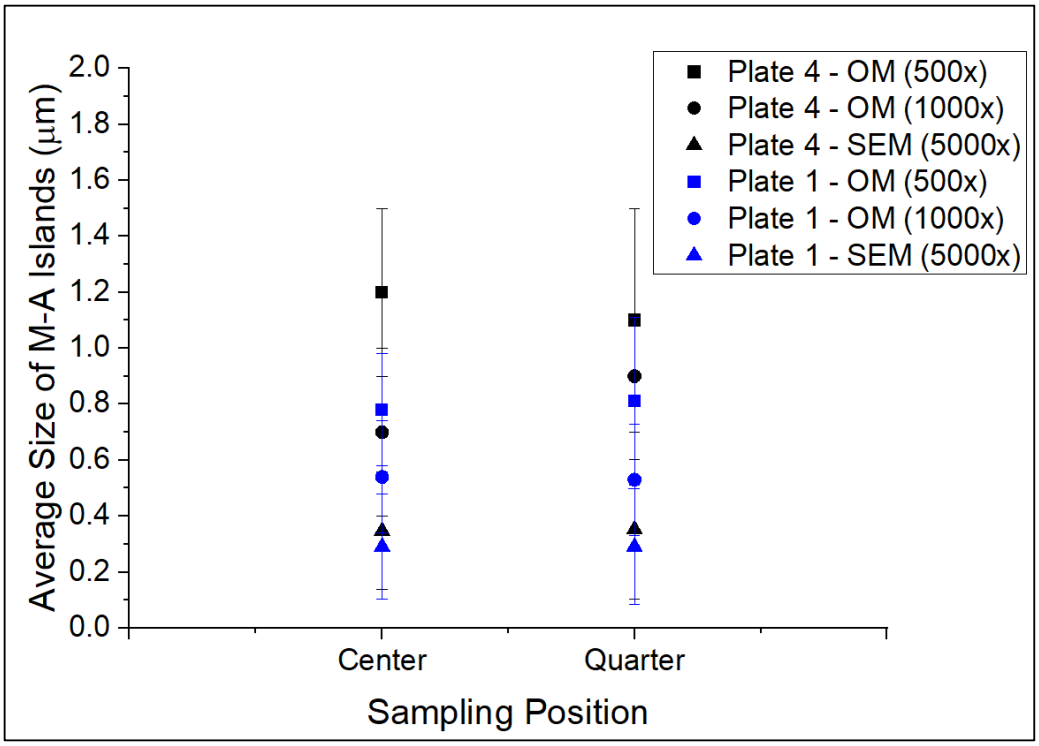

Figure 13. Comparison between the average sizes of M-A islands (average equivalent diameter) measured at the central and 1/4 thickness positions of plates 4 and 1 using optical micrographs at 500× and 1000× magnifications, and through scanning electron microscopy at 5000× magnification.

It was already noticeable in Figures 9 and 10 that the M-A islands, apparently, are more refined in plate 1, both in the center and at the ¼ thickness position. It can be confirmed that the fraction of M-A islands with an equivalent diameter of less than 0.3 μm is higher in plate 1, resulting in a smaller average, as highlighted in Figure 13.

In this context, it is assumed that, by observing both the fraction and size distribution data of M-A constituent islands, plates 4 and 1 have similar characteristics, both in the central region and at the ¼ thickness position. Some important points are highlighted: (i) the distribution of M-A islands is relatively homogeneous along the thickness for both plates; (ii) the fractions of M-A constituent are relatively low and homogeneous along the

thickness for both plates; (iii) the size distribution of M-A islands is relatively homogeneous along the thickness of both plates, with the islands of plate 1 being slightly more refined than those observed in plate 4; and (iv) apparently, the characterization of M-A constituent performed at this stage of the present work points to the hypothesis that it is not plausible that significant differences in mechanical behavior between plates 4 and 1, as shown later, are justified by differences related to the fraction and size of M-A islands.

Nevertheless, the literature states that in steels with a chemical composition similar to the one studied here, the fraction, size, and morphology of M-A islands can be strongly affected by the cooling rate and the austenite decomposition temperature into bainite. According to some authors, in general, lower cooling rates and higher final accelerated cooling temperatures favor the formation of coarser islands (blocks), which are preferentially formed at the boundaries of granular bainite units. This is a consequence of more favorable conditions for carbon diffusion during the bainitic transformation, allowing the intersection of relatively coarse regions highly enriched in carbon at the transformation front. These regions are conducive to the occurrence of martensitic transformation to a small extent and the consequent thermodynamic and mechanical stabilization of untransformed austenite, thus giving rise to blocky M-A constituent islands. For higher cooling rates and lower bainitic transformation temperatures, displacive mechanisms become more predominant in the bainite growth. Therefore, carbon diffusion will be shorter in range, resulting in less carbon enrichment between bainitic ferrite crystals. This scenario will favor the refinement of M-A islands, as well as the greater occurrence of film morphology [15,57,58].

3.5. Microstructural Characterization Results—SEM-EBSD

Figure 14 depicts maps of crystallographic disorientation for boundaries with disorientation angles less than 2° (kernel average misorientation—KAM maps) of plates 2 and 3, along with their mean kernel disorientation parameters (ϑ). Despite the two plates being subjected to different rolling strategies, it is noteworthy that they exhibited identical average kernel disorientation values (ϑ = 1.4°).

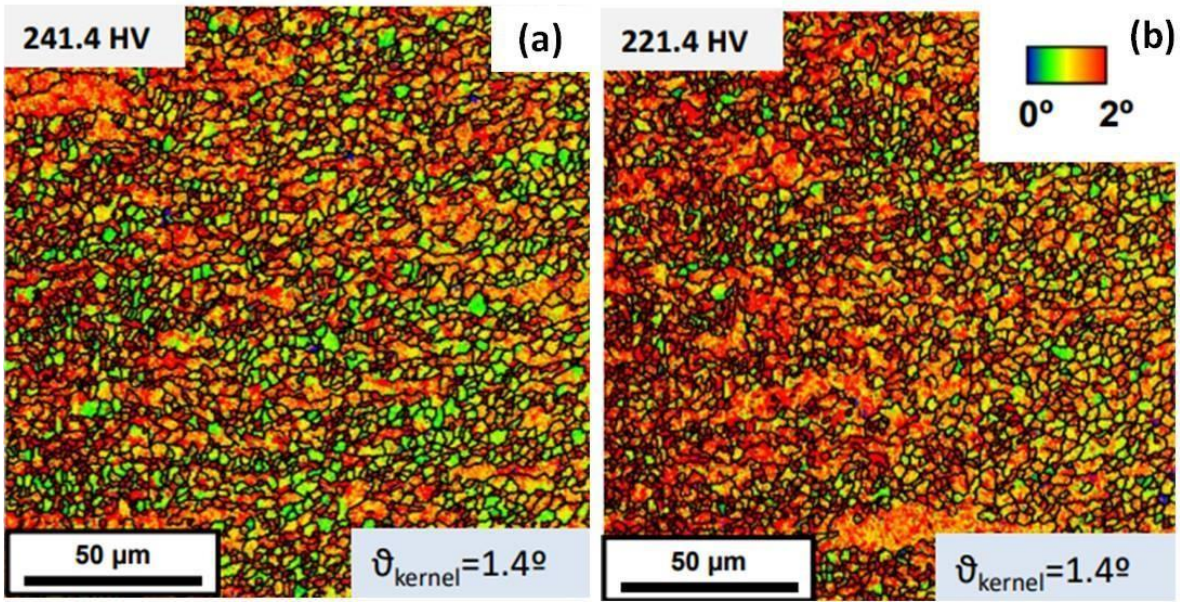

Figure 14. KAM maps—crystallographic disorientation maps considering $\vartheta < 2°$ for plates (**a**) 3 and (**b**) 2.

Despite the mean kernel misorientation parameter being the same for both plates, it is evident that the fraction of crystals with green coloring ($0.5° < \theta < 1°$) is significantly larger in plate 3 than in plate 2. According to Isasti et al. [25], intervals of grain boundaries with a crystallographic misorientation angle less than 2° ($\theta < 2°$) contribute to the work-

hardening mechanism by dislocation density, meaning that a higher local misorientation angle implies a higher dislocation density. In this context, Isasti et al. [25] suggest that a significant portion of crystals with $0.5° < \theta < 1°$ (green coloring) would be associated with primary ferritic structures, especially coarser ones indicating the presence of polygonal ferrite. Furthermore, in Figure 14a, it is observed that many crystals, possibly polygonal ferrite, are side by side, aligned in the rolling direction.

Figure 15 presents the grain boundary maps ($\theta > 4°$) of plates 2 and 3. Low-angle boundaries ($4° < \theta < 15°$) are highlighted in red. It is noticeable that in plate 2, the density of low-angle boundaries is higher than in plate 3. Particularly noteworthy is the presence of some relatively coarse regions, delimited by high-angle boundaries, with a high density of low-angle boundaries within. According to Larzabal et al. [56], a higher presence of low-angle boundaries strongly indicate a higher fraction of bainitic structures and nonpolygonal constituents, especially bainitic ferrite bundles formed at relatively high temperatures, nucleated from a few crystallographic variants.

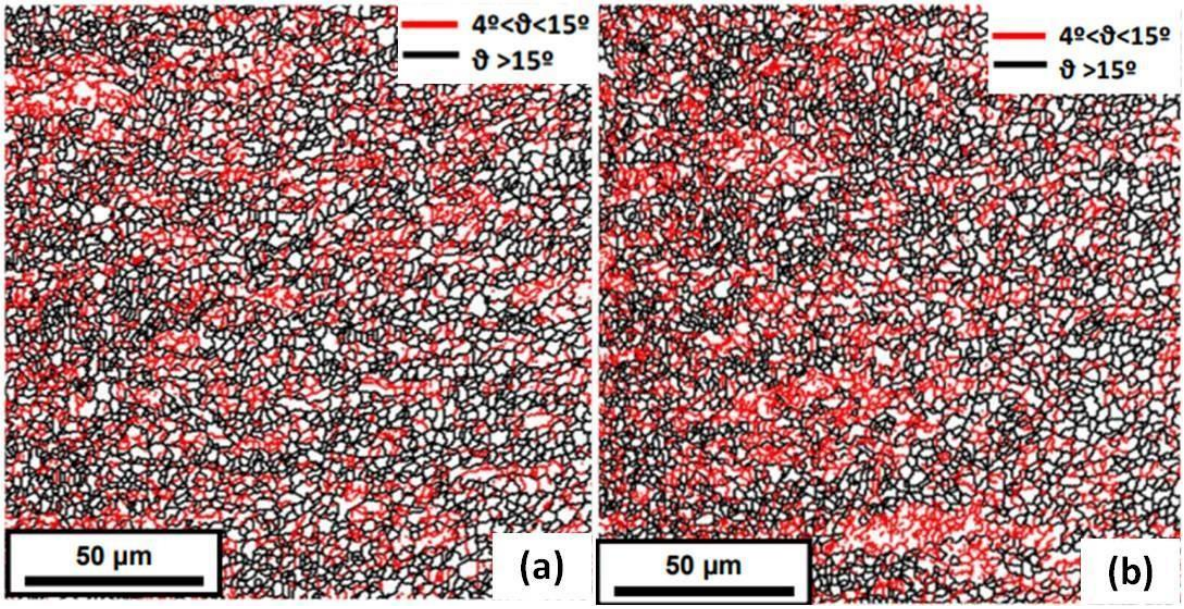

Figure 15. Grain boundary maps ($\theta > 4°$) of plates (**a**) 3 and (**b**) 2.

Table 4 and Figure 16 present the mean grain sizes of plates 2 and 3 considering threshold angles of 4° and 15°. For both criteria, it is evident that there is no significant difference in the average grain sizes.

Table 4. Mean grain sizes for plates 2 and 3 subjected to preliminary rolling conditions.

Plates	Average Size (µm)—4° Disorientation Criterion	Average Size (µm)—15° Disorientation Criterion
2	2.4	3.0
3	2.3	2.9

However, according to Cizek et al. [49], since plate 3 underwent a higher cumulative deformation at lower temperatures, a smaller austenitic grain size is expected at the beginning of accelerated cooling. This results in a higher density of preferred sites for the nucleation of diffusional constituents, accelerating the kinetics of austenite decomposition and raising the temperatures A_{r3} and A_{r1} for the same cooling rate. Generally, this acceleration in the kinetics of austenite decomposition, due to the smaller austenitic grain size, leads to a shift in the steel's CCT diagram to the left, favoring the formation of polygonal ferrite with very small grains in low carbon microalloyed steels.

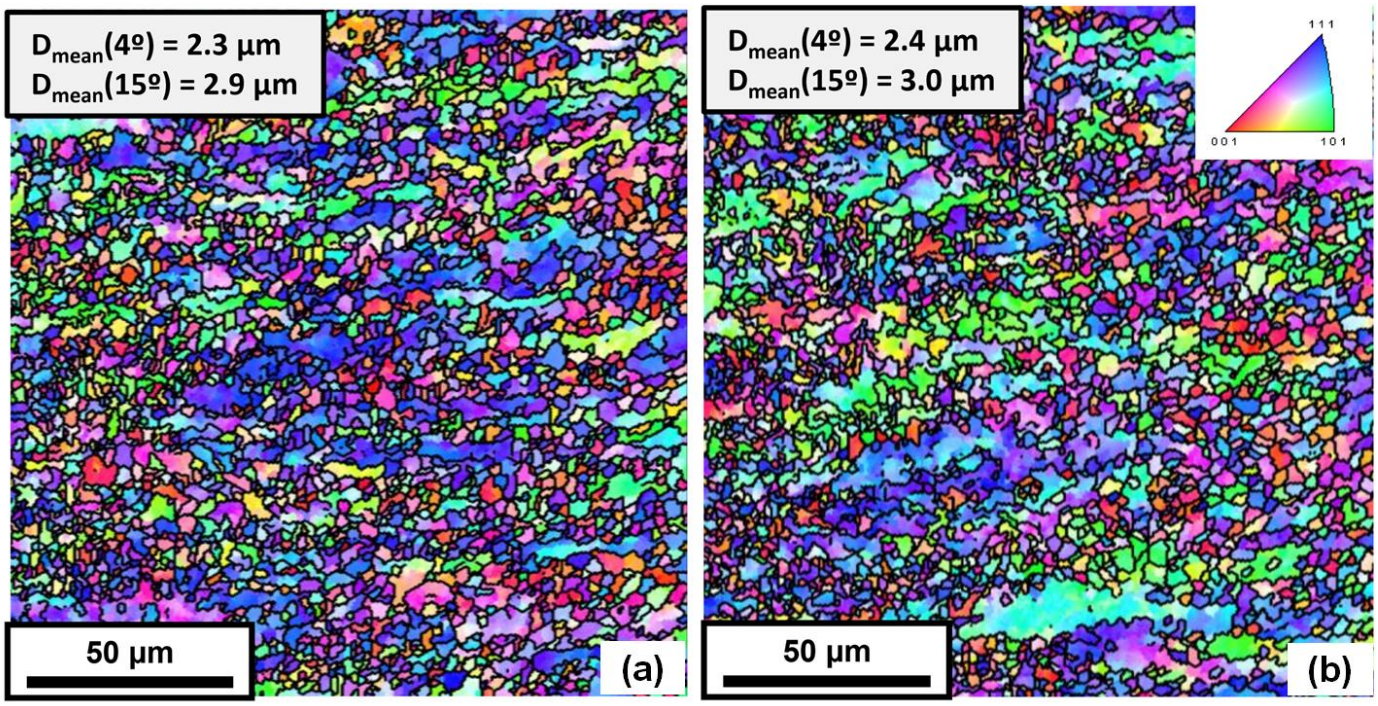

Figure 16. Inverse pole figures of plates (**a**) 3 and (**b**) 2.

In this scenario, a delicate balance seems to have been achieved. While the higher density of discontinuities may contribute to microstructural refinement by increasing the density of nucleation sites, the driving force for the transformation is also higher. This causes the austenite decomposition to start at higher temperatures, resulting in a larger critical nucleation radius. This may allow the formation of polygonal ferrite with relatively coarse grains compared to the average structure. Considering this subtle balance discussed, it appears that even though plate 3 underwent finishing rolling at lower temperatures, it did not effectively contribute to the microstructural refinement of the final product when compared to plate 2.

Using the EBSD characterization data and yield strength (σ_y) data obtained from tensile tests, the different contributions of hardening mechanisms were evaluated. The yield strength of low-carbon and microalloyed steels can be mathematically expressed by a function that considers various contributions, as shown by Equation (7).

Figure 17 presents the prediction of contributions from different hardening mechanisms to the tensile yield strength of plates 2 and 3.

Considering the results presented in Figure 17, it is noticeable that, due to very similar chemical compositions, as shown in Table 1, the contributions of solid solution strengthening in plates 2 and 3, calculated by Equation (8), are similar, measuring 137 MPa and 143 MPa, respectively.

Analyzing the results presented in Table 1 and Figure 15, one can understand that the effect of microstructural refinement on the yield strength of plates 2 and 3 would be similar. According to Equation (9), for plates 2 and 3, they would be 355 MPa and 363 MPa, respectively. It can be observed from Figures 14 and 15 that the microstructure of plate 3 appears slightly more refined than plate 2; hence, it is confirmed that the contribution of this microstructural refinement mechanism is subtly higher. According to Isasti et al. [25], the grain size reduction (Hall–Petch) hardening mechanism was the most relevant in all cases evaluated by them in Nb-Mo microalloyed steels, consistent with the results estimated in this study.

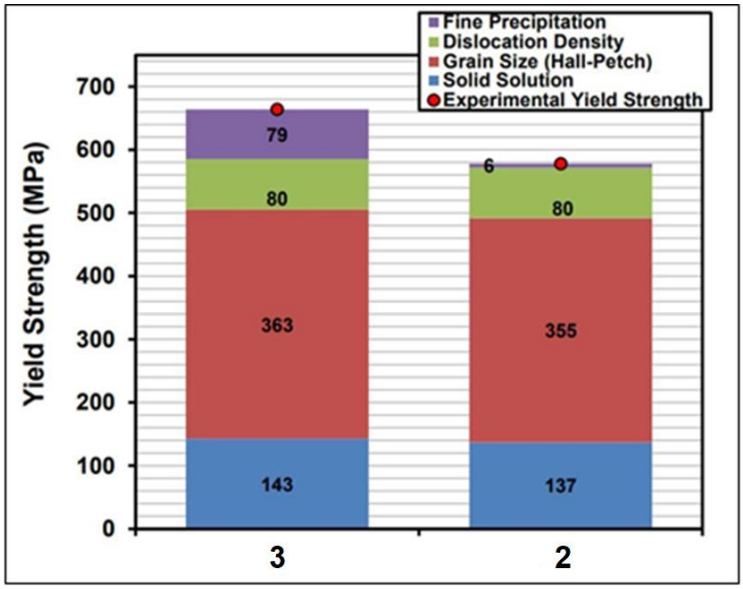

Figure 17. Prediction of contributions from different strengthening mechanisms to the tensile yield strength of plates 3 and 2. The red points correspond to the experimental tensile yield strength (Section 2.5).

However, even though plate 3 underwent finishing rolling passes at lower temperatures, as indicated in Table 3, this did not effectively contribute to the microstructural refinement of the final product when compared to plate 2. This result leads to an important cautionary note: the application of finishing rolling passes at relatively low temperatures, aiming to accumulate a higher density of structural discontinuities in the alloy for obtaining more refined bainitic microstructures, was not effective. On the contrary, this strategy enables the formation of a significant fraction of polygonal ferrite, mainly aligned in regions of negative Mn segregation, which may represent points of heterogeneity in the material, without a significant gain in the microstructural refinement hardening mechanism.

Regarding the dislocation density, as highlighted in Figure 14, since the average kernel misorientation parameter is the same for both plates (ϑ = 1.4°), by observing Equations (10) and (11), it was expected that the contributions from this mechanism would be identical for both plates (80 MPa).

Since the effect of the M-A constituent fraction was not considered, given its negligible quantity, as presented earlier, the only remaining contribution to justify the yield strengths of plates 2 and 3 was the precipitation hardening mechanism. In this context, this mechanism is considered to have contributed 79 MPa in plate 3, while contributing only 6 MPa in plate 2.

According to Edmonds [59], during finishing rolling, there may be the precipitation of carbides with equivalent diameters between 100 nm and 10 nm. These relatively coarse carbides would not have a significant effect on material hardening to justify an increase of almost 80 MPa in plate 3. However, there may be precipitation of carbides with sizes between 10 nm and 1 nm during the accelerated cooling stage, and these could indeed justify this significant contribution to the yield strength of the studied steel. Additionally, according to DeArdo [60,61], as the deformation applied to plate 3 occurred at lower temperatures, it may affect the kinetics of the formation and distribution of fine precipitates in the structure during accelerated cooling.

Another factor, according to Hu et al. [62] and Mohrbacher [63], in steels with chemical compositions similar to those presented in Table 1 used in this study, depending on the processing condition, intense formation of (Nb, Mo) (C, N) type precipitates may occur. Moreover, molybdenum inhibits the coalescence of these carbides by segregating at the matrix–carbide interface, favoring their refinement at the end of processing.

3.6. Mechanical Properties Results

The mechanical properties resulting from the rolling strategies are presented in Table 5.

Table 5. Mechanical properties obtained from two distinct rolling strategies (averages).

Rolling Strategy	Plate	Charpy Impact Energy (J)	YS—0.5% (MPa)	TS (MPa)	Elongation (%)	YS/TS	Hardness (HV)
B	3	301	664	708	42	0.94	235
	4	494	623	688	43	0.91	202
A	2	478	578	671	42	0.86	228
	1	490	583	712	43	0.82	217

The two rolling strategies produced notably distinct mechanical properties, particularly evident in the yield strength, where plate 3 exhibited the highest result. It is noteworthy that rolling Strategy B resulted in a remarkably high elastic ratio (YS/TS), exceeding 0.91, whereas the maximum allowed for the final product, according to the API 5L X80 standard, is 0.93. Consequently, for plate 3, the elastic ratio of the heavy plate product already surpasses the maximum tolerance specified in the API 5L X80 standard [48].

Concerning the toughness outcomes of rolling Strategy B, plate 3 demonstrated the least favorable performance in Charpy impact tests (at −20 °C). In this strategy, after finishing rolling, an austenitic structure with a higher dislocation density is expected, especially in plate 3. Coupled with relatively low cooling rates during the accelerated cooling step, this could lead to microstructural heterogeneity due to the presence of polygonal ferrite. Despite plate 4 exhibiting more apparent heterogeneity under light microscopy, its Charpy impact results outperformed those observed in plate 3.

In a previous study [25], the mechanical properties of API 5L X80 pipes were evaluated, and the authors concluded that these properties, especially tensile strength (TS) and toughness, show a strong correlation with equivalent carbon content (EC). In this study, plate 3 came from a batch with slightly higher EC_{Pcm} values than the batch that produced plate 4.

Concerning rolling Strategy A, the values of yield strength (YS), tensile strength (TS), and impact toughness were within the specified range [48]. Notably, plate 1 exhibited the best balance between mechanical strength and impact toughness, along with the lowest elastic ratio among the four rolled plates. Plate 2 showed a slightly coarser microstructure than plate 1, which justifies the minor differences observed in mechanical properties under tension and Charpy impact toughness between the two plates of rolling Strategy A.

The TS and elongation values obtained meet the specifications for heavy plates intended for API 5L X80 pipes [48]. Remarkably, rolling Strategy A yielded the highest impact toughness values at −20 °C, along with the highest elongation values across all plates.

Regarding hardness values presented in Table 3, unlike the YS results, there is no discernible trend between the two rolling strategies. While the API 5L standard does not specify hardness values for general-purpose PSL level 2, it does set a maximum hardness of 300 HV for grade X80 in offshore applications (Annex J in the Standard). Thus, considering the values obtained in the four rolled plates, the hardness of the finished product would remain within the limit, even for more stringent applications [48].

4. Conclusions

Both rolling strategies met all critical temperatures, rolling conditions, and accelerated cooling requirements, except for the finishing rolling final temperature in one of the strategies and the average rate of accelerated cooling in three out of the four plates.

Microstructural characterization by optical microscopy (OM) and scanning electron microscopy (SEM) confirmed that the final steel microstructure adhered to the proposal, predominantly consisting of granular bainite. The presence of Mn segregation bands in the

central regions, where the presence of polygonal ferrite was confirmed, was also identified. Additionally, the presence of M-A constituents was nearly insignificant.

Characterization by SEM-electron backscatter diffraction (EBSD) confirmed similar values for both conditions. Thus, the difference found between the plates in terms of their mechanical properties was associated with the precipitation hardening mechanism.

Mechanical testing results confirmed that all conditions met the requirements for compliance with the API 5L grade X80 standard, considering the manufacturing of heavy plates with a final thickness of 20.66 mm, especially for Strategy A. Furthermore, noteworthy were the good results for elongation in the transverse direction to the rolling and the absorbed energy results.

Finally, contrary to what is classically described for controlled-rolled low-alloy steels manufactured by controlled rolling, Strategy B, which had an austenitic structure with a higher density of sites for the nucleation of diffusional constituents, led to the formation of a significant fraction of primary ferrite during the accelerated cooling stage. This was due to deformation at lower finishing temperatures, especially in regions of the heavy plate subjected to lower cooling rates and with negative manganese segregation.

Considering the obtained results, it is possible to affirm that the proposed Strategy A parameters can be successfully used to manufacture API 5L X80 heavy plates in a reversible single-stand mill. It is important to advertise that it is not recommended to accumulate extremely high deformation in austenite during the finishing rolling (70% is the highest suggested). The last finishing pass should not occur at a temperature lower than Ar_3 + 90 °C.

Author Contributions: Conceptualization, L.G.d.O.A., R.R.P. and G.L.d.F.; methodology, G.L.d.F., L.G.d.O.A. and R.R.P.; software, R.J.d.F. and D.B.M.; validation, R.R.P., G.L.d.F. and L.G.d.O.A.; formal analysis, G.L.d.F. and R.R.P.; investigation, L.G.d.O.A., R.R.P. and G.L.d.F.; resources, L.G.d.O.A., R.J.d.F. and D.B.M.; writing—original draft preparation, L.G.d.O.A.; writing—review and editing, all; supervision, R.R.P. and G.L.d.F.; project administration, L.G.d.O.A., R.J.d.F. and D.B.M.; funding acquisition, R.J.d.F. and D.B.M. All authors have read and agreed to the published version of the manuscript.

Funding: This research was partially funded by Gerdau S.A.

Data Availability Statement: The data presented in this study are available on request from the corresponding author. The data are not publicly available due to privacy and industrial confidentiality.

Acknowledgments: The authors thank Gerdau S.A. for financial support and CEIT and UFOP for the steel characterization tests and technical support.

Conflicts of Interest: Authors Luiz Gustavo de Oliveira Abreu, Ricardo José de Faria and Daniel Bojikian Matsubara were employed by the company Gerdau Ouro Branco. The remaining authors declare that the research was conducted in the absence of any commercial or financial relationships that could be construed as a potential conflict of interest.

References

1. Saboia, R.H. (General Director) ANP—Anuário Estatístico Brasileiro do Petróleo, Gás Natural e Biocombustíveis; Agência Nacional do Petróleo, Gás Natural e Biocombustíveis, Rio de Janeiro, Brazil. 2021; ISSN 1983-5884. Available online: https://www.gov.br/anp/pt-br/centrais-de-conteudo/publicacoes/anuario-estatistico/arquivos-anuario-estatistico-2021/anuario-2021.pdf (accessed on 23 May 2024).
2. Saboia, R.H. (General Director) ANP—Anuário Estatístico Brasileiro do Petróleo, Gás Natural e Biocombustíveis; Agência Nacional do Petróleo, Gás Natural e Biocombustíveis, Rio de Janeiro, Brazil. 2022; ISSN 1983-5884. Available online: https://www.gov.br/anp/pt-br/centrais-de-conteudo/publicacoes/anuario-estatistico/arquivos-anuario-estatistico-2022/anuario-2022.pdf (accessed on 23 May 2024).
3. Al-Sabaeei, A.M.; Alhussian, H.; Abdulkadir, S.J.; Jagadeesh, A. Prediction of oil and gas pipeline failures through machine learning approaches: A systematic review. *Energy Rep.* **2023**, *10*, 1313–1338. [CrossRef]
4. Liao, Q.; Liang, Y.; Tu, R.; Huang, L.; Zheng, J.; Wang, G.; Zhang, H. Innovations of carbon-neutral petroleum pipeline: A review. *Energy Rep.* **2022**, *8*, 13114–13128. [CrossRef]
5. Zhou, D.; Jia, X.; Ma, S.; Shao, T.; Huang, D.; Hao, J.; Li, T. Dynamic simulation of natural gas pipeline network based on interpretable machine learning model. *Energy* **2022**, *253*, 124068. [CrossRef]

6. Ravago, M.V.; Fabella, R.V.; Jandoc, K.R.; Frias, R.G.; Magadia, J.K.P. Gauging the market potential for natural gas among Philippine manufacturing firms. *Energy* **2021**, *237*, 121563. [CrossRef]
7. Laureys, A.; Depraetere, R.; Cauwels, M.; Depover, T.; Hertelé, S.; Verbeken, K. Use of existing steel pipeline infrastructure for gaseous hydrogen storage and transport: A review of factors affecting hydrogen induced degradation. *J. Nat. Gas Sci. Eng.* **2022**, *101*, 104534. [CrossRef]
8. Zhang, H.; Li, S.; Ding, W. Study on the continuous cooling transformation behavior of heavy thickness X80 pipeline steel. *IOP Conf. Ser. Mater. Sci. Eng* **2019**, *631*, 022014. [CrossRef]
9. Guo, K.; Pan, T.; Zhang, N.; Meng, L.; Luo, X.; Chai, F. Effect of microstructural evolution on the mechanical properties of Ni-Cr-Mo ultra-heavy steel plate. *Materials* **2023**, *16*, 1607. [CrossRef] [PubMed]
10. Wang, Q.; Ye, Q.; Tian, Y.; Fu, T.; Wang, Z. Superior Through-Thickness Homogeneity of Microstructure and Mechanical Properties of Ultraheavy Steel Plate by Advanced Casting and Quenching Technologies. *Steel Res. Int* **2021**, *92*, 2000698. [CrossRef]
11. Julio, C.; Li, W.; Ke, J.; Xu, Y.; Pang, H.; Jin, X. Study of the impact properties and microstructure evolution in a high-strength low-alloy heavy steel. *Mater. Sci. Eng. A* **2021**, *819*, 141404. [CrossRef]
12. Gorni, A.A.; Silveira, J.H.D.; Reis, J.S.S. Um Panorama do Desenvolvimento Recente de Chapas Grossas e suas Aplicações. *Corte Conform. Met.* **2006**, *2*, 78–93.
13. Martins, C.A.; Faria, G.L.; Mayo, U.; Isasti, N.; Uranga, P.; Rodriguez-Ibabe, J.M.; Souza, A.L.; Cohn, J.A.C.; Rebellato, M.A.; Gorni, A.A. Production of a non-stoichiometric Nb-Ti HSLA steel by thermomechanical processing on a steckel mill. *Metals* **2023**, *13*, 405. [CrossRef]
14. Pourazizi, R.; Mohtadi-Bonab, M.A.; Davani, R.K.Z. Effect of thermo-mechanical controlled process on microstructural texture and hydrogen embrittlement resistance of API 5L X70 pipeline steels in sour environments. *Int. J. Press. Vessel. Pip.* **2021**, *194*, 104491. [CrossRef]
15. Faria, G.L.; Porcaro, R.R.; Godefroid, L.B.; Cândido, L.C.; Faria, R.J. Development of heavy plates API 5L Grade X80—Thermomechanical control processing. *Tecnol. Metal. Mater. Mineração* **2024**, *21*, e3038. [CrossRef]
16. Wu, Z.; Yang, W.; Tang, Z.; Siyasiya, C.W.; Zhang, J. Thermomechanical control of microstructure and precipitation in vanadium microalloyed steel: Influence of finish rolling and coiling temperatures. *Steel Res. Int.* **2024**, *95*, 2300478. [CrossRef]
17. Soeiro Junior, J.C.; Rocha, D.B.; Brandi, S.D. Uma breve revisão histórica do desenvolvimento da soldagem dos aços API para tubulações. *Soldag. Inspeção* **2013**, *18*, 176–195. [CrossRef]
18. Kim, K. Effect of Microalloying and Hot Rolling Parameters on Toughness and Yield Strength of API X80 Grade Steel Strips. In Proceedings of the Symposium on Fundamentals and Applications of Mo and Nb Alloying in High Performance Steels, Taipei, Taiwan, 7–8 November 2014; pp. 135–153.
19. Machado, F.R.S.; Ferreira, J.C.; Rodrigues, M.V.G.; Lima, M.N.S.; Loureiro, R.C.P.; Siciliano, F.; Silva, E.S.; Reis, G.S.; Sousa, R.C.; Aranas, C.; et al. Dynamic ferrite formation and evolution above Ae3 temperature during plate rolling simulation of an API X80 steel. *Metals* **2022**, *12*, 1239. [CrossRef]
20. Omale, J.I.; Ohaeri, E.G.; Mostafijur, K.M.; Szpunar, J.A.; Arafin, M. Through-Thickness Inhomogeneity of Texture, Microstructure, and Mechanical Properties After Rough and Finish Rolling Treatments in Hot-Rolled API 5L X70 Pipeline Steel. *J. Mater. Eng. Perform.* **2020**, *29*, 8130–8144. [CrossRef]
21. Xu, L.; Qiao, G.; Gong, X.; Gu, Y.; Xu, K.; Xiao, F. Effect of through-thickness microstructure inhomogeneity on mechanical properties and strain hardening behavior in heavy-wall X70 pipeline steels. *J. Mater. Res. Technol.* **2023**, *25*, 4216–4230. [CrossRef]
22. Zurutuza, I.; Isasti, N.; Detemple, E.; Schwinn, V.; Mohrbacher, H.; Uranga, P. Effect of Nb and Mo additions in the microstructure/tensile property relationship in high strength quenched and quenched and tempered boron steels. *Metals* **2021**, *11*, 29. [CrossRef]
23. Wu, Q.; He, S.; Hu, P.; Liu, Y.; Zhonghua, Z.; Fan, C.; Fan, R.; Zhong, N. Effect of finish rolling temperature on microstructure and mechanical properties of X80 pipeline steel by online quenching. *Mater. Sci. Eng. A* **2023**, *862*, 144496. [CrossRef]
24. Lino, J.J.P. Laminação Controlada de um Aço Microligado ao Nióbio Visando a Obtenção do Grau API X60 em Laminador Steckel. Master's Thesis, Universidade Federal de Ouro Preto, Ouro Preto, Brazil, 2017.
25. Isasti, N.; Jorge-Badiola, D.; Taheri, M.L.; Uranga, P. Microstructural features controlling mechanical properties in Nb-Mo microalloyed steels. *Part I: Yield Strength. Met. Mater. Trans. A* **2014**, *45*, 4960–4971. [CrossRef]
26. Cui, S.; Gu, G.; Shi, C.; Xiao, G.; Lu, Y. Variations in microstructure and mechanical properties along thickness direction in a heavy high strength low alloy steel plate. *J. Mater. Res. Technol.* **2023**, *26*, 9190–9202. [CrossRef]
27. Roccisano, A.; Nafisi, S.; Stalheim, D.; Ghomashchi, R. Effect of TMCP rolling schedules on the microstructure and performance of X70 steel. *Mater. Charact.* **2021**, *178*, 111207. [CrossRef]
28. Conde, F.F.; Pina, F.J.; Giarola, J.M.; Pereira, G.S.; Francisco, J.C.; Avila, J.A.; Bose, W.W. Microstructure and mechanical properties of Nb-API X70 low carbon steel. *Metallogr. Microstruct. Anal.* **2021**, *10*, 430–440. [CrossRef]
29. Qiao, G.Y.; Chen, X.W.; Zhang, Z.E.; Han, X.L.; Wang, X.; Liao, B.; Xiao, F.R. Mechanical properties of high-Nb X80 steel weld pipes for the second west-to-east gas transmission pipeline project. *Adv. Mater. Sci. Eng.* **2017**, *2017*, 7409873. [CrossRef]
30. Gorni, A.A. Aspectos metalúrgicos da solubilização de microligantes durante o reaquecimento de placas de aço. In Proceedings of the 65° Congresso ABM, Rio de Janeiro, Brazil, 26–30 July 2010.
31. Irvine, K.J.; Pickering, F.B.; Gladman, T. Grain-Refined C-Mn STEELS. *J. Iron Steel Inst.* **1967**, *205*, 161–182.
32. Nodberg, H.; Arronson, B. Solubility of Niobium Carbide in Austenite. *J. Iron Steel Inst.* **1968**, *206*, 1263–1266.

33. Hudd, R.C.; Jones, A.; Kale, M.N. A Method for Calculating the Solubility and Composition of Carbonitride Precipitates in Steel with Particular Reference to Niobium Carbonitride. *J. Iron Steel Inst* **1971**, *209*, 121–125.
34. Kong, X.; Lan, L. Optimization of mechanical properties of low carbon bainitic steel using TMCP and accelerated cooling. *Procedia Eng.* **2014**, *81*, 114–119. [CrossRef]
35. Uranga, P.; Rodriguez-Ibabe, J.M.; Stalheim, D.G.; Barbosa, R.A.N.M.; Rebellato, M.A. Application of Practical Modeling of Microalloyed Steels for Improved Metallurgy, Productivity and Cost Reduction in Hot Strip Mill Applications. In Proceedings of the Aistech—Iron and Steel Technology Conference, Pittsburgh, PA, USA, 16–19 May 2016.
36. Rosado, D.B.; De Waele, W.; Vanderschueren, D.; Hertelé., S. Latest developments in mechanical properties and metallurgical features of high strength line pipe steels. *Int. J. Sustain. Constr. Des.* **2013**, *4*, 1–10. [CrossRef]
37. *ASTM E3-11*; Standard Guide for Preparation of Metallographic Specimens. ASTM International: West Conshohocken, PA, USA, 2017.
38. *ASTM Designation E112*; Standard Test Methods for Determining Average Grain Size. American Society for Testing and Materials: West Conshohocken, PA, USA, 2021.
39. *ASTM E1245-03*; Standard Practice for Determining the Inclusion or Second Phase Constituent Content of Metals by Automatic Image Analysis. ASTM International: West Conshohocken, PA, USA,, 2016.
40. *ASTM E562-19*; Standard Test Method for Determining Volume Fraction by Systematic Manual Point Count. ASTM International: West Conshohocken, PA, USA, 2020.
41. *ASTM E1382-97*; Standard Test Methods for Determining Average Grain Size Using Semiautomatic and Automatic Image Analysis. ASTM International: West Conshohocken, PA, USA, 2015.
42. Pickering, F.B.; Gladman, T. *Metallurgical Developments in Carbon Steels*; Special Report No. 81; Iron and Steel Inst.: London, UK, 1963.
43. Iza-Mendia, A.; Gutiérrez, I. Generalization of the existing relations between microstructure and yield stress from ferrite-perlite to high strength steels. *Mater. Sci. Eng. A* **2013**, *561*, 40–51. [CrossRef]
44. Kubin, L.P.; Mortensen, A. Geometrically necessary dislocations and strain-gradient plasticity: A few critical issues. *Scr. Mater* **2003**, *48*, 119–125. [CrossRef]
45. Zurutuza, I.; Isasti, N.; Detemple, E.; Schwinn, V.; Mohrbacher, H.; Uranga, P. Effect of Quenching Strategy and Nb-Mo Additions on Phase Transformations and Quenchability of High-Strength Boron Steels. *J. Miner. Met. Mater. Soc. (TMS)* **2021**, *73*, 3158–3168. [CrossRef]
46. *ASTM Designation A370*; Standard Test Methods and Definitions for Mechanical Testing of Steel Products. American Society for Testing and Materials: West Conshohocken, PA, USA, 2021.
47. *ASTM Designation E92*; Standard Test Methods for Knoop and Vickers Hardness of Materials. American Society for Testing and Materials: West Conshohocken, PA, USA, 2023.
48. *API—American Petroleum Institute-Specification for Line Pipe*, 46th ed.; API Publishing Services: Washington, DC, USA, 2018.
49. Cizek, P.; Wynne, B.; Davies, C.; Muddle, B.; Hodgson, P. Effect of Composition and Austenite Deformation on the Transformation Characteristics of Low-Carbon and Ultralow-Carbon Microalloyed Steels. *Met. Mater. Trans. A* **2002**, *33*, 1331–1349. [CrossRef]
50. Liu, C.; Shi, L.; Liu, Y.; Li, C.; Li, H.; Guo, O. Acicular ferrite formation during isothermal holding in HSLA steel. *J. Mater. Sci.* **2016**, *51*, 3555–3563. [CrossRef]
51. Adel, A.A. Modelamento da Transformação de Fases de Aços de Alta Resistência Microligados ao Nb durante Resfriamento após Laminação em Tiras a Quente. Ph.D. Thesis, Universidade Federal de Minas Gerais, Belo Horizonte, Brazil, 2007.
52. Guo, H.; Zhou, P.; Zhao, A.; Zhi, C.; Ding, R.; Wang, J. Effects of Mn and Cr contents on microstructures and mechanical properties of low temperature bainitic steel. *J. Iron Steel Res. Int.* **2017**, *24*, 290–295. [CrossRef]
53. Takekazu, A.; Kimihiro, N.; Koji, Y.; Nobuhisa, S. Development of High Performance UOE Pipe for Linepipe. *JFE Tech. Rep.* **2013**, *18*, 23–35.
54. Laitinen, R. Improvement of weld HAZ toughness at low heat input by controlling the distribution of M-A constituents. Ph.D. Thesis, Oulu University, Oulu, Finland, 2006.
55. Hrivnak, I.; Matsuda, F.; Ikeuchi, K. Investigation of M-A constituent in high strength steel welds. *Trans. JWRI* **1992**, *21*, 149–171.
56. Larzabal, G.; Isasti, N.; Rodriguez-Ibabe, J.M.; Uranga, P. Evaluating strengthening and impact toughness mechanisms for ferritic and bainitic microstructures in Nb, Nb-Mo and Ti-Mo microalloyed steels. *Metals* **2017**, *7*, 65. [CrossRef]
57. Zhao, H.; Wynne, B.P. Effect of austenite grain size on the bainitic ferrite morphology and grain refinement of a pipeline steel after continuous cooling. *Mater. Charact.* **2017**, *123*, 128–136. [CrossRef]
58. Chang, L.C.; Bhadeshia, H.K.D.H. Metallographic observations of bainite transformation mechanism. *Mater. Sci. Technol.* **1995**, *11*, 106–108. [CrossRef]
59. Edmonds, D.V. Designing with microalloyed and interstitial-free steels. In *Handbook of Mechanical Alloy Design*; George, E.T., Lin, X., Kiyoshi, F., Eds.; Marcel Dekker Inc: New York, NY, USA, 2004; pp. 321–353.
60. DeArdo, A.J. Niobium in modern steels. *Int. Mater. Rev.* **2003**, *48*, 371–402. [CrossRef]
61. DeArdo, A.J. The Metallurgy of High Strength Linepipe Steels. In Proceedings of the Symposium on the Pipelines for the 21st Century, Calgary, Canada, 21–24 August 2005.

62. Hu, H.; Xu, G.; Wang, L.; Xue, Z.; Zhang, Y.; Liu, G. The effects of Nb and Mo addition on transformation and properties in low carbon bainitic steels. *Mater. Des.* **2015**, *84*, 95–99. [CrossRef]
63. Mohrbacher, H. Synergies of niobium and boron microalloying in molybdenum based bainitic and martensitic steels. In *Fundamentals of Applications of Mo and Nb Alloying in High Performance Steels—Volume 1—Proceedings of the First International Symposium on Fundamentals and Applications of Mo and Nb Alloying in High Performance Steels, Taipei, Taiwan, 7–8 November 2011*; Hardy, M., Ed.; CBMM: Amsterdam, The Netherlands; IMOA: London, UK; TMS: Frederick, MD, USA, 2014; ISBN 978-0-615-67631-9.